Electronic Transport in Lithium Nickel Manganese Oxide, a High-Voltage Cathode Material for Lithium-Ion Batteries

By

Alan Patrick Adams Ransil

B.S. Materials Science and Engineering (2010)
Stanford University

Submitted to the Department of Materials Science and Engineering
in Partial Fulfillment of the Requirements for the Degree of

Master of Engineering in Materials Science and Engineering
at the
Massachusetts Institute of Technology

February 2013

Signature of Author

Department of Materials Science and Engineering
December 5, 2012

Certified by

Yet-Ming Chiang
Kyocera Professor of Materials Science and Engineering
Thesis Supervisor

Accepted by

Gerbrand Ceder
R. P. Simmons Professor of Materials Science and Engineering
Chair, Departmental Committee on Graduate Students

Electronic Transport in Lithium Nickel Manganese Oxide, a High-Voltage Cathode Material for Lithium-Ion Batteries

By

Alan Patrick Adams Ransil

Submitted to the Department of Materials Science and Engineering
on December 12, 2012 in Partial Fulfillment of the Requirements for Degree of
Master of Engineering in Materials Science and Engineering

ABSTRACT

Potential routes by which the energy densities of lithium-ion batteries may be improved abound. However, the introduction of Lithium Nickel Manganese Oxide ($Li_xNi_{1/2}Mn_{3/2}O_4$, or LNMO) as a positive electrode material appears to be one of the shortest. LNMO is a high-voltage material, with a voltage of 4.7V, and thus offers a significant energy density boost without straying far outside of the stability window of common carbonate-based electrolytes. Furthermore, it would serve as a drop-in replacement for the positive electrode materials already used. In order to best engineer such devices to take full advantage of the intrinsic transport properties of the material, it is important to develop an understanding of what these transport properties are. For a deep understanding of the material such properties must be related not only to material performance but to the processing conditions and atomic structure of the material. The material may be processed such that it belongs in either the $P4_332$ or the Fd3m space group, exhibiting either order or disorder respectively of Ni and Mn cations. Such processing has a great effect on the concentrations of electronic charge carriers, and thus an effect on the DC electronic conductivity of the material. This conductivity was thus measured for both processing conditions as a function of the lithiation state, and then related to carrier concentrations via the small polaron model for charge conduction. In such a way, the links betweer processing, structure and properties of this material were elucidated. It is hoped that this work will be built upon in order to engineer the high energy-density batteries of the future.

Thesis Supervisor: Yet-Ming Chiang
Title: Kyocera Professor of Material Science and Engineering

ACKNOWLEDGEMENTS

I want to thank my adviser, Yet-Ming Chiang, for his guidance throughout my Master's thesis. I have learned a lot from the Chiang group about electrochemical energy storage during my time here, especially from Billy Woodford. Ruhul Amine has taught me a tremendous amount about charge transport measurements, and we have had many fruitful conversations on LNMO in particular. Thank-you to Dorthe Bomholdt Ravnsback for performing Rietveld analyses on some of my data, and access to a huge depth of knowledge about diffraction experiments. David Young was a fantastic lab mate with whom I worked on charge transport in spinels, porous electrode models, and Van Der Pauw setup construction. Thank-you as well to Kai Xiang, with whom I often discuss the battery industry and who provided a water kettle which made possible the coffee which made readily available the caffeine without which science could not be done.

My friends at MIT have been a constant source of inspiration, commiseration, innovation, conversation, and elation. Thank-you especially to Wenhao Sun who has helped me to learn, teach, speak publically and better understand my context within the larger world; Rae Zucker whose honest, forthcoming and incisive opinion will readily get to the foundation of nearly any issue; Deepak Jagannathan whose broad interests and ability to see the big picture invariably bring up a new and valuable perspective when discussing any topic; Nancy Twu who brings people together with astounding alacrity; Tim Milakovich who enjoys life; Kunal Mukherjee whose skepticism inspires better experimental design; and David Cohen-Tanoudji whose conversations over lunch, coffee, dinner and drinks are always welcome.

My friends from undergrad continue to help me do better work. Especially thank-you to Jason Law, whose zeal for three-dimensional campus voyages helped me learn to appreciate universities and who helps me figure out what's worth doing and how to go about it. Thank-you to Juan Ignaçio Antonio Ramón Batiz-Benet for all of the champagne.

Thank-you to my family, who have given me the life I have. Thank-you to my Mom, for helping me to understand that bottom-up architectures are more powerful on every level than top-down, for teaching me how to make things happen, and for giving me the courage to admit when something isn't working and to try something different. Thank-you to my Dad, who has always built things with me, who has taught me to love science, and has made it second nature for me to think on a high level about the world and how to fix it. Thank-you to my Brother, who dives into everything he does and helps me to do the same.

Especially thank-you to my girlfriend Chelsea, who cares deeply about the same things that I do, shares them all with me, and who never ceases to be a source of warmth and inspiration.

TABLE OF CONTENTS

LIST OF FIGURES

LIST OF TABLES

H. I. INTRODUCTION

A. The Promise of Lithium Nickel Manganese Oxide

Electrochemical energy storage is thought to be a nearly 2000 year old technology,[1] but its advances have been slow and hard won. As a result, progress in battery science often holds back that in other technologies ranging from power grid load leveling to portable mobile devices. The electric automobile is one of the technologies with the greatest global significance suffering from this problem. Cheaper batteries with high energy densities are urgently needed to spur widespread adoption of the electric car in order to stave off global warming.

Among strategies for improving energy density is increasing the voltage of the 'active material' electrochemical couple. This comes down to choosing the positive electrode from a set of materials giving more energy per unit of capacity. Since these would be lithium intercalation materials similar to those in existing batteries, they could potentially be used as drop-in replacements. This would increase battery energy density without requiring any re-tooling of production facilities. Thus, high-voltage electrode materials are considered part of the potential 'low-hanging fruit' of battery science. However, current carbonate-based electrolytes decompose at high voltages. This continues to present challenges to the implementation of these materials.

Of high-voltage materials, Lithium Nickel Manganese Oxide ($Li_xNi_{1/2}Mn_{3/2}O_4$, or LNMO) is likely the nearest to commercialization. It is made by adding Nickel to the common Lithium Manganese Oxide ($LiMn_2O_4$, or LMO) spinel. The Nickel replaces Manganese as the electrochemically active ion, pushing the voltage plateau up by about 15% to 4.7V. This voltage is relatively low compared to other high-voltage materials under development (which are 5+ volts), which causes this material to decompose electrolyte more slowly. This also makes electrochemical studies much easier.

The United States Advanced Battery Consortium (USABC), an industry group dedicated to promoting research to electrify automotive drivetrains, has published a series of goals for Battery Electric

Vehicles (BEVs) and Plug-in Hybrid Electric Vehicles (PHEVs).[2] These are taken as technical targets for pack-level electrochemical storage systems which would allow electric vehicles to become cost-competitive with traditional petrol-powered automobiles. LNMO could likely achieve the high-power PHEV targets for energy density and power density[3] should the electrolyte decomposition issue be dealt with.

The Batteries for Advanced Transportation Technologies (BATT) program sponsored by the Department of Energy has launched a research effort focused on LNMO in order to achieve a broad and deep understanding of its properties. As part of this research effort, the present work has studied electronic conductivity in the material.

Due to the nature of ion intercalation in lithium-ion batteries, an active material (such as LNMO) must be accessible at all points to both electrons and ions. In conventional cells, ions are supplied by the electrolyte. Electrons, by contrast, must be supplied by the current collector and make their way through the solid cathode. Most cathode materials are not conductive enough to support these currents at a high rate, so an electronic conductor (usually carbon black) is mixed into the electrode during processing. Carbon is only about half as dense as a typical transition metal oxide, so this electrochemically inactive additive can significantly lower the volumetric capacity of the electrode. Understanding charge transport in active materials thus may allow us to better engineer high-voltage electrodes for the energy storage devices of the future. In order to achieve a full understanding of LNMO conduction behavior, one must consider the atomic origin of transport. LNMO has two transition metal cations which, depending on processing conditions, may both be electrochemically active. This makes it a rich electrochemical system and gives rise to its complex conduction properties.

B. Scope of the Thesis

The goal of the present work is to measure the electronic conductivity of LNMO as a function of lithiation, and to relate this to structure and processing conditions. The literature includes information about the structure-processing relationship, and relates this to the electronic conductivity of the fully lithiated spinel. However, there is no published data about the evolution of electronic conductivity as the material is delithiated. This represents a serious hole in the knowledge of the transport properties of LNMO, as its electronic conductivity is thus not well known over the range of compositions actually sampled in a battery.

To do this, temperature-dependent four-point probe measurements were performed on LNMO samples electrochemically delithiated to a range of charge states. This was done on LNMO prepared using two different sintering conditions in order to result in samples of both 'Ordered' $P4_332$ and 'Disordered' $Fd\bar{3}m$ polymorphs. As documented in the literature, (see review below) these polymorphs differ electrochemically and have different electronic conductivities in their fully lithiated states. Their conductivities were shown in this work to evolve differently as delithiated.

Electronic conductivity and activation energy were thus related to sample composition and the electrochemical behavior of both polymorphs of LNMO.

II. IMPROVING ELECTROCHEMICAL ENERGY STORAGE

a. The Principle Behind Li-Ion Batteries

Modern-day battery technology traces its roots to the experiments of Alessandro Volta in the early nineteenth century. A voltaic cell is an electrochemical device in which a redox reaction between metals of different electronegativity is separated by an electrically insulating electrolyte. As one electrode reacts, it produces cations which travel across the electrolyte towards the second electrode. Electrons are forced in the same direction through a wire, and charge balance is maintained at each electrode. A modern lithium ion battery using the 'rocking chair' design (Figure 2.1) is similar except that the reactant does not fully dissolve into the electrolyte. On discharge, lithium ions dissolve out of the anode, cross the electrolyte, and intercalate into the cathode.

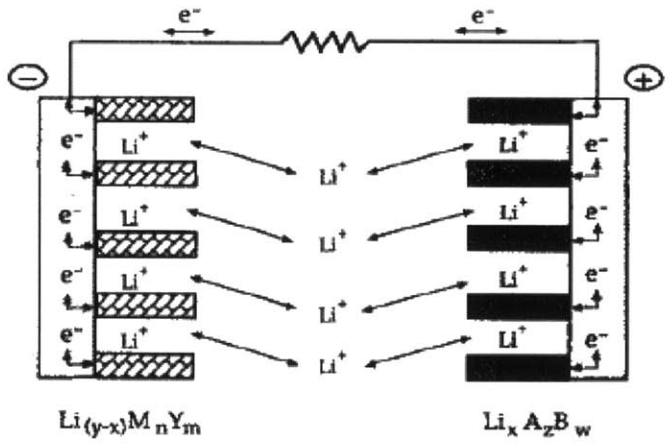

Figure 2.1: This image shows a diagram of the 'rocking chair' design of modern rechargeable lithium-ion batteries. Two lithium intercalation compounds are connected so that Li^+ ions but not electrons may communicate between them through the battery. Electrons are forced to take an outside path, doing work. (From Reference 4)

Thus the Anode discharge half-reaction is

$$LiAnode \rightarrow Anode + e^- + Li^+$$

While the cathode accepts the Li ion and the electron to perform the half-reaction:

$$Cathode + e^- + Li^+ \rightarrow LiCathode$$

Thus only a small fraction of the electrode must be dissolved in and cross the cell, leaving the bulk of both electrodes stationary. This leads to fast kinetics (rate capability) and relatively good stability (cycle life), as entire electrodes need not be dissolved and reconstituted with each cycle. In principle, for a wide range of intercalation materials, this reaction is electrochemically reversible with a small overpotential. To power this reaction, materials have been discovered with great differences in lithium intercalation energy. This allows high energy densities to be achieved relative to other electrochemical energy storage systems.

This intercalation design, however, faces several intrinsic challenges. Firstly, most materials undergo vegard strain when intercalated with lithium, expanding by several volume percent. This strain can cause structural damage. Secondly, many materials are stable in one structure when lithiated but transform into a second phase when delithiated (these include Lithium Cobalt Oxide and Lithium Titanate). Thirdly, this is intrinsically a multi-phase system which generally involves a liquid electrolyte. It is difficult to find solvents which are stable over a sufficiently wide electrochemical window. This is a particular problem for high-voltage electrodes such as LNMO. Fourth, the energy density of known systems with well-understood properties conducive to large-scale manufacture is lower than the value required for easy commercialization of electric cars, and significantly too low for the production of battery-powered large-scale aircraft. This is a materials problem, which will likely be solved by discovering electrode couples with higher energy densities. Novel architectures may also enable better energy densities by decreasing the amount of inactive material in a cell or by increasing cell size. (For a discussion of the packaging of cells and why larger cells may improve performance, see the following section.)

b. Metrics employed in the study of lithium ion batteries

Charge and discharge rates are generally measured using the 'C-rate' convention. This states a rate as C/x where x is the number of hours required to fully (dis)charge the cell to the theoretical capacity

at the stated rate. Thus, a C/5 rate will (dis)charge in 5 hours while a 10C rate will (dis)charge the cell in 6 minutes.

Gravimetric capacity of a cell or of an active material is generally measured in units of mAh/g. This is the amount of charge that can be released from one gram of material, assuming full (de)lithiation for the 'theoretical' capacity of the material. Several caveats are attached to this idea. Firstly, while the theoretical capacity is a fixed value, the value realized (or nominal) in practice will vary with C-rate. Generally, a voltage cutoff is determined and a battery is cycled within a determined voltage range. At high rates, the polarization will increase. This will cause the cell to hit its voltage cutoff before reaching the theoretical capacity. Thus high rates result in a lower nominal capacity. The picture is further complicated by the fact that some battery materials such as Lithium Cobalt Oxide become structurally unstable when delithated past a given state of lithiation. In the case of LCO, the material is never cycled past ~50% delithiation as it will irreversibly degrade. Thus, a reversible gravimetric capacity of137 mAh/g is often quoted as the 'theoretical' capacity of LCO despite the fact that full delithiation would correspond to 274 mAh/g.

The voltage of a cell varies with state of charge, despite the fact that a set voltage is often quoted for a given material such as 4.7V for LNMO. Generally the quoted voltage corresponds to that of a voltage plateau when measured in an electrochemical 'half cell' using a lithium anode. When paired with graphite or silicon, the voltage of the overall cell will be approximately 0.5V lower than that quoted.

Energy density is measured in Wh/kg (gravimetric energy density) or Wh/L (volumetric energy density). This number corresponds to the average voltage of a cell multiplied by its capacity. Energy density is always a property of an electrochemical cathode/anode couple rather than that of an individual active material. Furthermore, one must specify whether one refers to the *materials level* energy density, the *cell level* energy density which includes other cell components such as current collectors and cell packaging, or – for automotive applications – the *pack level* energy density of the overall energy storage

unit inserted into the vehicle. To demonstrate this difference, Table 2.1 presents the materials-level, cell-level and pack level efficiencies of industry batteries for which public information is available. In this analysis it is assumed that the cells are based on an NMC/graphite couple.

	Gravimetric Energy Density	**Volumetric Energy Density**
Theoretical Materials Level (NMC/Graphite Couple)	557 Wh/kg	1800 Wh/L
Cell Level (Panasonic 18650)	236 Wh/kg (42% of materials-level)	620 Wh/L (34% of materials-level)
Pack Level (Nissan Leaf, Chevrolet Volt)	120 Wh/kg (51% of cell)	100 Wh/L (16% of cell)

Table 2.1 demonstrating differences between various energy density figures. (From Reference 3)

Another battery property, cycle life, is the number of electrochemical cycles which a battery can be expected to undergo while remaining in good operating condition. In industry, this is generally taken to mean the number of cycles which a cell may be subjected to with its capacity falling not below 90% of its initial value. This is a cell-level quantity, but the origins of degradation upon cycling lie at the materials level. Electrode cracking due to vegard strain and electrolyte side reactions are two of the main factors contributing to degradation. In LNMO, electrolyte side reactions lead to a low cell cycle life as commercial electrolytes are not stable at 4.7V. This is the primary problem in the commercialization of LNMO.

c. **Comparing energy densities of Active Materials**

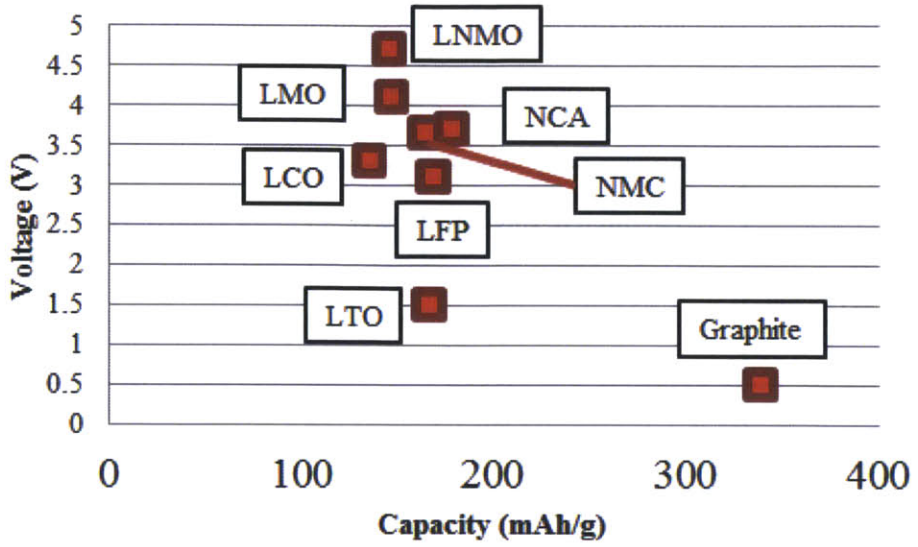

Figure 2.2 Voltages and capacities of common active materials for lithium-ion batteries. Capacity is either the theoretical capacity if it can be achieved reversibly, or the maximum reversible capacity otherwise.

Figure 2.2 demonstrates the voltages and capacities of many active materials commonly used and studied in lithium-ion batteries. As voltage times capacity is energy density, positive electrode materials positioned to the right and higher on the chart will result in higher energy density batteries. This chart demonstrates the case for LNMO: not only does the material have a reasonable capacity, but it has the highest voltage of any material being considered for the present as a battery active material. Its voltage is about 15% higher than Lithium Manganese Oxide (LMO) and 29% higher than NMC, leading to sizeable potential improvements in energy density. Furthermore, because its voltage is so high, the cell voltage lost due to the use of an anode material at a higher potential than lithium robs the electrochemical couple of proportionally less energy.

It should be noted that the possible improvements to the negative electrode side of the cell are limited. Graphite, at 0.5V, is at the lowest potential considered safe for use in commercial cells. At lower potentials the risk of lithium plating at high rates becomes significant which could result in dendrites short-circuiting the battery. Graphite also has a very high capacity compared to positive electrode materials, and with the introduction of Silicon (at a similar voltage to graphite) the negative electrode

capacity has the potential to increase by a factor of 2x in the near-term and 8x in the long term. Thus, battery researchers hoping to maximize their impact should focus on positive electrode materials for the present.

d. State-of-the-Art Cell Architecture

As Motivation for LNMO Charge Transport Study

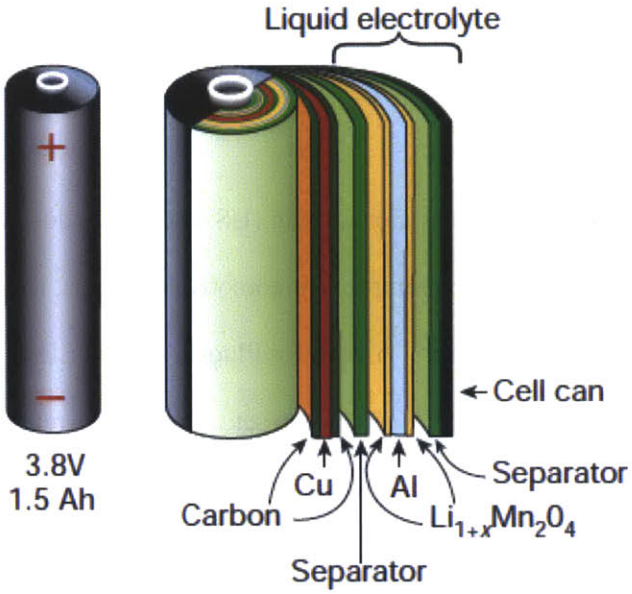

Figure 2.3: This is the basic design on which modern commercial secondary (ie. rechargeable) lithium-ion batteries are based. Electrode material (carbon and LMO in this example, but in general a wide range of intercalation materials may be used) are coated onto Cu and Al current collectors. These are wound with a separator to result in a high surface-area taking advantage of roll-to-roll processing techniques. (From *Reference #5*)

Modern battery production has been highly optimized by industry. Cells are produced by first coating a slurry of active material and other additives onto foil, resulting in a thin electrode in contact with a current collector. The resulting anode and cathode rolls are then wound up with a separator between them. This results in a cell architecture similar to that in figure 2.3. Such an architecture achieves high surface area, allowing rapid ion transport between the electrodes.

In this architecture the high surface area required and the low electrode thickness results in the final cell being approximately just under 60 mass% and just over 60 volume% active material (*Appendix*

D). The remaining mass and volume are devoted to inactive components such as the current collectors, separator and cell casings, which is considered a drawback as these materials do not directly contribute to cell capacity. However, this architecture allows the use of roll-to-roll processing, promoting ease of high-volume manufacture. This suggests that it will be difficult to scale an alternative cell architecture at a competitive price point. Thus a significant research effort will continue to be expended on 'drop-in' replacements for current active materials, which will allow higher energy densities without requiring significant changes in cell manufacture. LNMO has the potential to be such a material.

e. USABC Goals

The United States Advanced Battery Consortium (USABC), an industry body interested in advancing electrochemical energy storage to improve automotive transport, has set a series of goals to serve as a focusing point for battery research. A each for Plug-In Hybrid Electric Vehicles (PHEVs) and fully battery-powered Electric Vehicles (EVs) have been set. These goals refer to the pack-level capabilities which the USABC believes will allow electric vehicle technology to become commercially competitive. As these goals refer to pack-level energy densities, we can use the estimates in Table 2.1 to compare the expected energy density of an LNMO system to these targets.

f. Routes for Improvement

There are several potential routes by which batteries may be improved which form active areas of current research. One of these is by implementing new battery architectures which might enable a higher loading of active material in the overall battery system, or might enable storage through novel electrochemical reactions. There has been recent interest, for example, on redox flow batteries based on traditional lithium-ion active materials. Such an architecture may enable battery systems consisting of a very high fraction of active material, as the current collectors occupy only a small fraction of the total system.[6,7,8] Lithium-air (or lithium-oxygen) batteries are another technology in which new architectures may enable higher energy density batteries but requires substantial further research.[9,10,11]

However, the 'low-hanging fruit' of advanced batteries relies on developing improved active materials which can be dropped in to existing battery architectures. Silicon anodes, for example, are a technology which has long been under development. Several recent advances appear on the verge of allowing this material to be incorporated into negative electrodes with little re-tooling of production equipment.[12,13] LNMO also falls into the drop-in replacement category. Its higher voltage would allow for better energy densities, but its operational principle is the same as those of other transition metal oxides used as positive electrodes in lithium-ion batteries today. However, for such a venture to prove successful, new electrolytes must be developed to improve the stability of the high-voltage electrochemical system.

Another route to improving electrochemical energy storage involves adjusting, rather than re-inventing, battery architectures to achieve higher active material loading. As shown in Appendix D, 3% of the overall cell volume is devoted to conductive carbon additive in the cathode. This allows electronic currents to traverse the electrode with low polarization. As lowering the volume of the cell is a high priority, it is important to consider active materials with improved electronic transport properties. Thus, accurate information on the electronic conductivity of an active material as a function of charge state is a vital piece of information in the consideration of new active materials.

Were an electrode material developed with sufficiently high electronic conductivity (over the range of lithiation states exhibited during cycling) to not require conductive additive, this would immediately allow the manufacture of denser electrodes and higher cell-level energy density. See image 2.3 for a plot of the active material conductivity required at various discharge rates. In this image, it is assumed that the electrode is an additive-free slab of active material with thickness as a variable graphed along the x-axis. Lines represent, for a given discharge rate, the electronic conductivity of the active material required in order to limit the polarization to a given value (set as a parameter in the legend). Given that modern battery electrodes are approximately 20μm thick, this plot serves as a guide as to the order of magnitude of intrinsic electronic conductivity required for an additive-free electrode to not be

limited by electronic resistance. It thus suggests that an active material with a conductivity of 10-3 S/cm would allow for thicker electrodes with higher active material loading. It is important to note that electrode porosity and binder are not considered in this plot.

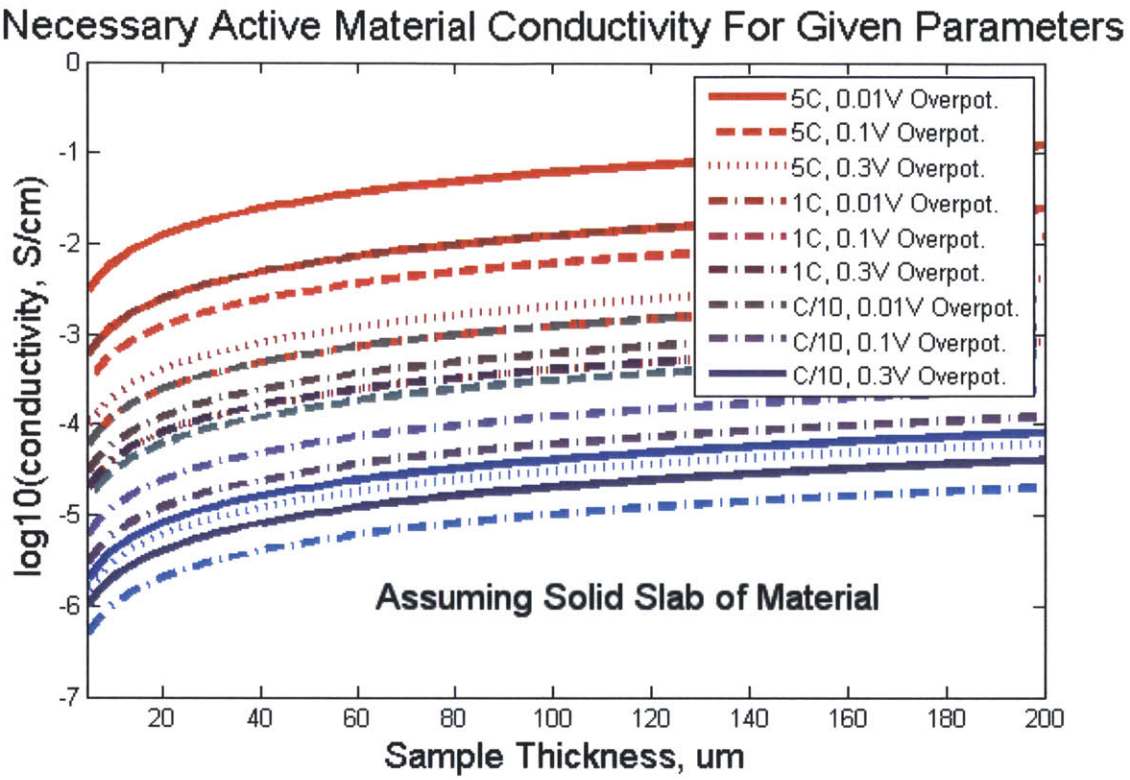

Figure 2.4: Minimum electronic conductivity required to limit polarization at a given C-rate, calculated as a function of sample thickness. This can be used to determine targets for active material conductivity in high-capacity electrodes. It should be noted that, as this plot assumes a solid slab of active material, electrode porosity and the presence of inactive binder will influence the require conductivity (though likely by only 10's of percentage points, for reasonable values of porosity and volume % binder).

Better understanding of electronic transport may thus allow us to engineer thicker electrodes with less conductive additive. When considering the electronic conductivity of a battery material, it is important to note that the conductivity – and thus the overall electrode resistance – will change as the electrode composition changes; for example, as the cell is lithiated. In metal oxides such as LNMO which conduct electrons by small polaron hopping, this is thought to be the result of the changing oxidation states of transition metal cations. These oxidation states change as the electrode is (de)lithiated in order to enforce local charge neutrality.

g. High-Voltage Positive Electrode Materials

As explained above, the benefit of high-voltage positive electrode materials is to achieve a larger energy density for a given battery capacity. The main problem facing this category of electrode materials is the instability of carbonate-based electrolytes at high voltages.

Pyrophosphates [14,15]

Lithium intercalation Pyrophosphates are materials with the chemical formula $Li_xMP_2O_7$, where M is a transition metal and x can be either 1 or 2. These materials can be high-capacity, particularly x=2 and the second lithium can be extracted, and high-voltage. The extraction of either one or both lithium ions in some pyrophosphates are of sufficiently high voltage that they are difficult to study experimentally using liquid electrolytes. As a result, the higher voltage plateaux have not been extensively studied experimentally. Expected voltages and energy densities of many compounds have, however, been predicted computationally, and would likely result in significant advances if they could be implemented (with, for example, an electrolyte tolerant of high voltages).

Tavorites[16]

These compounds are isostructural to $LiFePO_4OH$, and include Oxysulfates, Fluorosulfates, Oxyphosphates and Fluorophosphates. Similarly to Pyrophosphates, some are capable of multiple lithium intercalation at high voltage. Also similar to pyrophosphates, the Tavorites often intercalate lithium at so high a voltage that it is not possible at this point to study their lithium intercalation experimentally using readily accessible electrolytes.

Lithium Nickel Manganese Oxide

Lithium Nickel Manganese Oxide (LNMO) is among the lowest of the high-voltage positive electrode materials being considered. At 4.7V, right at the edge of the electrolyte stability window, it is considered to be the closest to commercialization. In order to better understand the challenges and promise of this material, it was chosen as a focus material of the Batteries for Advanced Transportation

Technologies (BATT) program run by the Department of Energy (DOE). The present study deals with the electronic transport component of this research effort.

III. Spinel-Structured Electrode Materials and Electronic Transport

a. Spinel Structured Oxides

Spinel is a vitreous mineral with the chemical formula $MgAl_2O_4$. It has the space group $Fd\bar{3}m$. In its unit cell, O^{2-} anions form an FCC lattice occupying all the 32e sites, while Al^{3+} and Mg^{2+} cations occupy half of the octahedral 16d and $1/8^{th}$ of the tetrahedral 8a sites, respectively. Minerals with this crystal structure are common, and their properties have been long studied. A special case of the spinel structure relevant to lithium ion batteries is that of LiM_2O_4, in which Li^+ ions occupy the tetrahedral 8a sites. In this case, the mineral goes from a structure like $Mg^{2+}Al^{3+}{}_2O_4$, in which the first metal has +2 valence, to one in which monovalent lithium replaces it. This forces the other metal into a higher valence state and, as in the case of $Li^+Mn^{3.5+}{}_2O_4$, it often adopts mixed valence.

b. Comparing layered and olivine to spinel electrode materials

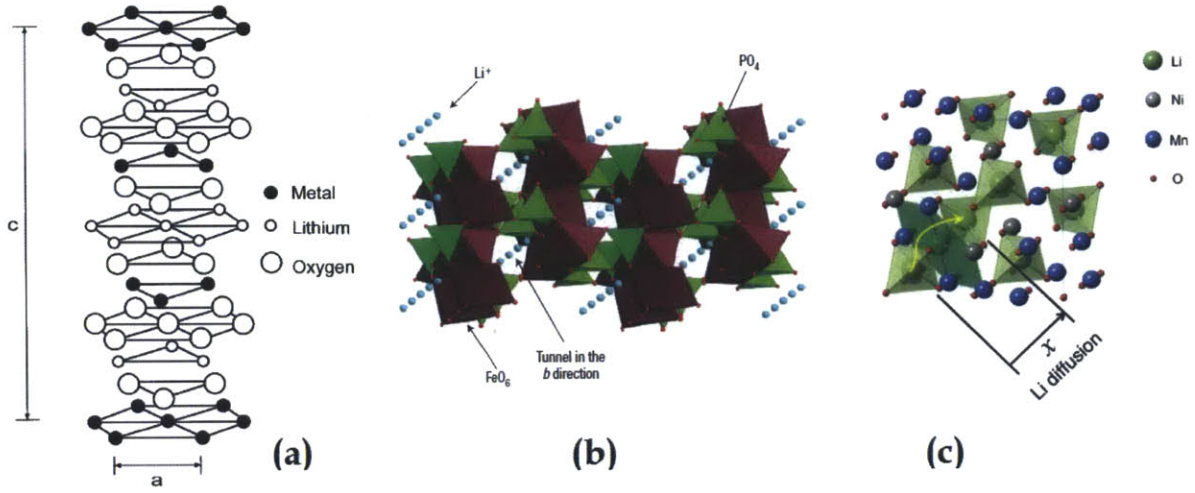

Figure 3.1: (a) The layered structure of LCO from reference 17; (b) the structure of LFP from reference 18 in which the one-dimensional lithium intercalation channels are apparent; (c) spinel structure of LNMO from 19 in which one possible ion jump is shown. It can be seen here that lithium ions in the spinel jump from one tetrahedral site to another through an adjacent octahedral site. Due to the low occupancy of these sites, the ion can move in three dimensions through the crystal.

Many compounds used as battery electrodes have either a layered or olivine structure. The layered structure (figure 3.1a) refers to compounds such as LCO and graphite (though the structures are

clearly not isomorphic), in which tight bonds are experienced within parallel plains and Li ions fit between these planes. Lithium intercalation causes the weaker out-of-plane bonds to lengthen, generally causing the material to expand anisotropically. As a result of this insertion mechanism, lithium ions within the material are generally confined to in-plane (two dimensional) motion, unable to traverse the sheets in the out of plane direction.

The olivine structure of many minerals, such as Lithium Iron Phosphate (LiFePO4, or LFP) is even more restrictive to lithium motion. Rather than being able to traverse in two dimensions, lithium ions in the olivine structure are confined to 1-d channels. These pathways can become blocked by stray ions if there is disorder in the lattice, causing the lithiation kinetics to be slow unless workarounds are implemented. Such workarounds come in the form small particle sizes – since there is simply a lower probability of a 1d channel being blocked if it is shorter – or the need to amorphize small bits of the material in order to provide alternate pathways for the Li.[20]

Spinels, by contrast, have three-dimensional ionic pathways penetrating the material. As a result, intercalated lithium ions can readily follow concentration and potential gradients and gain access to the entire body of active material. The result is good lithium diffusion (as discussed at length below in the case of LNMO).

c. Examples of spinel-structured Lithium Intercalation Oxides

Lithium Titanate

Lithium Titanate, or LTO, is an advanced negative electrode material used in some commercial cells. The delithiated form contains lithium ions in both the 8a and 16d positions, sharing the 16d with titanium. Upon lithiation, it undergoes the reaction:

$$Li_4Ti_5O_{12} + 3Li^+ + 3e^- \rightarrow Li_7Ti_5O_{12}$$

During lithiation, the 16d position cations remain stationary while the 8a ions switch into the 16c sites. This transforms the material from the spinel to the rocksalt structure. Having 168 mAh/g

theoretical capacity, this material is a good lithium intercalator by the standards of transition metal oxides. The primary benefit to using this material is that the vegard strain upon lithiation is only about 0.1%,[21,22] much less than that of other active materials, which leads to little physical damage to the crystal during cycling.[23]

The relatively high intercalation voltage of 1.5V has both benefits and drawbacks. The benefit is that an SEI does not form on the material, as it does for traditional anode materials at 0.5V. The drawback is that this lowers the overall cell voltage. Pairing LTO with LNMO is thus a potentially attractive option, and has been proposed.[24],[25]

Lithium Manganese Oxide

With the formula LiMn2O4, Lithium Manganese Oxide (LMO) and its derivatives are commonly used in commercial cells. LMO itself is a '4V' electrode material with a theoretical capacity of 148 mAh/g. The spinel structure accommodates a wide range of transition metal cations, so Mn can be substituted with other elements in varying quantities to tune the properties of the electrode. A common LMO-based derivative is NMC, or Lithium Nickel Manganese Cobalt Oxide. While compositions made by different producers may vary, a typical composition might be LiNi0.85MnCo0.15O4. At about 170 mAh/g and a voltage of ~3.7V, NMC is often the positive electrode material of choice for high energy-density commercial batteries.

Lithium Nickel Manganese Oxide

Similarly to NMC, Lithium Nickel Manganese oxide is based on substituting Mn with other transition metal cations while retaining a spinel structure. The resulting material has a composition of $LiNi_{0.5}Mn_{1.5}O_4$ and a capacity of 147 mAh/g, with a voltage of 4.7V. This is considered a high-voltage material, as it is beyond the electrochemical stability window of carbonate-based electrolytes. However, it is only just beyond that window (as compared to many tavorites and pyrophosphates which have intercalation potentials of >5V). Thus, electrolyte decomposition is too high as yet for commercialization

but proceeds slowly enough that these electrodes can studied using conventional electrolytes. The material has thus become a focus for research into high-voltage electrodes. It forms the subject of this thesis, and will be discussed at length in proceeding sections.

d. Charge Transport in Oxides

A priori, we would expect the small polaron conduction mechanism to govern electronic charge transport in LNMO. This has been well studied in similar spinel-structured transition-metal oxide spinels such as Magnetite (Fe_3O_4)[26,27,28] and Manganese Oxides. [29,30,31,32]

A polaron is a charge carrier which travels through a lattice along with its strain field. Small polarons in particular are well-localized to single atoms, and must travel between lattice sites via thermally activated hopping. Small polaron transport has extensively been both worked out in theory[33,34] and verified experimentally[35,36,37,38] The general equation governing conductivity in a small polaron system is:

$$\sigma_{SP} = \sigma_0 e^{\frac{-E_\mu}{kT}} = c\,(1-c)\frac{q^2 a^2 \nu}{kT}\, e^{\frac{-E_\mu}{kT}}$$

Here, a is the hop distance between sites and ν is the lattice vibrational frequency at which jumps are attempted. T, k, e and q are absolute tempearature, Boltzmann's constant, the mathematical constant, and the polaron charge respectively. E_μ is an activation energy (see below). c is the concentration of polarons and 1-c the concentration of potential hopping sites. Thus if a Mn^{3+} is a polaron site in LNMO, the concentration of Mn^{3+} would be c and the concentration of Mn^{4+} would be 1-c. This equation has several important features.

The initial part of the equation, $c(1-c)q^2a^2\nu/kT$, is the conductivity estimated from diffusivity theory. This can be seen by using the Einstein relation to transform the diffusivity into a mobility, then using $\sigma = \rho\mu$ (in which these variables represent conductivity, charge density and mobility respectively) in order to derive the conductivity. The final term in this equation, $\exp[-E_\mu/kT]$, is easily recognized as being of the Arrhenius form for thermally activated processes in which an activation barrier must be

overcome. The activation energy E_μ is the mobility activation energy, or the energy of the transition state corresponding to the small polaron hopping between two ionic cores. This involves not only a potential energy barrier for the electron, but any drag effects due to the strain component of the polaron.

In order to evaluate conductivity data in light of this theory, the data are often presented as an Arrhenius Diagram featuring 1/T on the horizontal axis and log(σ) on the vertical (see figure 3.3, an Arrhenius diagram from the literature showing the electronic conductivity of fully lithiated LNMO for different sintering conditions). This makes it straightforward to compare both overall conductivity and the mobility activation energy of the systems plotted, corresponding to the value and the negative inverse slope of the lines on the diagram respectively.

Material	**Structure**	**Hopping Energy**	**Source**
$LiMn_2O_4$	Spinel	0.268 eV – 0.342 eV (function of sintering conditions and off-stoichiometry)	Reference 39
CeO_{2-x} $0.008<x<0.25$	Fluorite	0.38 eV – 0.52 eV	Reference 36
$NiFe_2O_4$	Inverse Spinel	0.43 eV	Reference 40

Table 3.1: Hopping energy of selected well-studied oxides exhibiting small-polaron conduction behavior

Electronic conductivity as a function of charge state has been published for LMO, and it is established to be a small-polaron conductor.[41,42] The author is aware of only one published dataset examining the electronic resistance of an additive-free LNMO electrode as a function of charge state,[43] and it does not claim to have adequately separated the active material resistance from other relevant effects.

IV. LITHIUM NICKEL MANGANESE OXIDE: STRUCTURE AND ELECTROCHEMISTRY

a. Voltage Profile

According to the Gibbs phase rule, a system at equilibrium (such as an electrode being very slowly lithiated) must satisfy:

$$D = C + 2 - P$$

Where D is the number of degrees of freedom, C is the number of components of the system, P is the number of phases (and 2 represents Temperature and Pressure, which must be specified as degrees of freedom). In a battery with lithium ions (component 1) diffusing through an active material (component 2), the number of phases will influence the voltage curve. If there is one phase, the degrees of freedom will include Temperature, Pressure and Voltage. If the material phase separates during equilibrium discharge, Voltage disappears as a degree of freedom and the cell will have only one voltage across the phase separated region[1]. Figure 4.1 shows the cycling curves of LMO-based compounds in which progressively more Ni is added. This results in the composition $LiNi_xMn_{1-x}O_4$.

[1] The converse is not necessarily true; ie. observing a nearly flat voltage curve does not necessarily mean the electrode material phase separates.

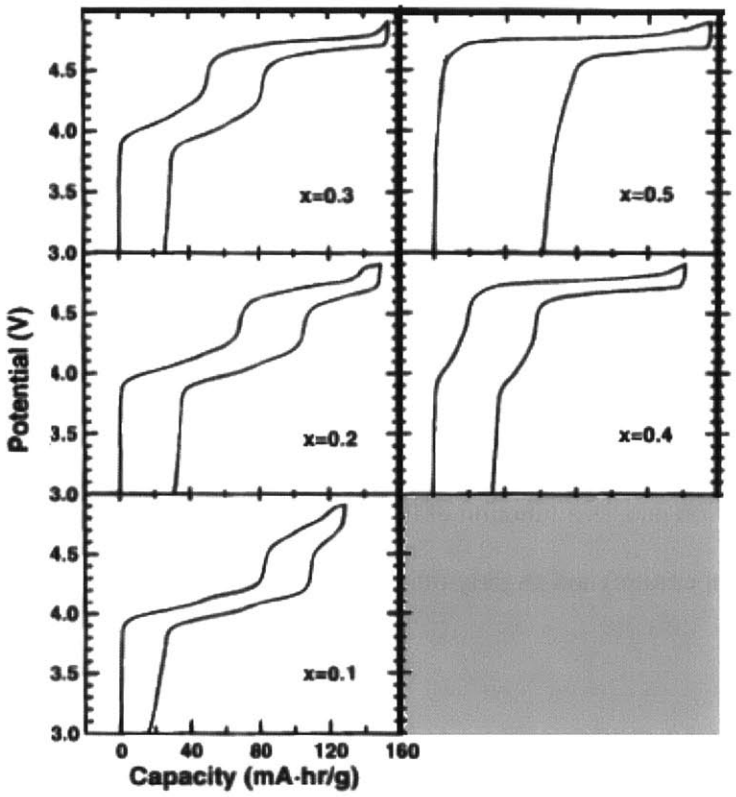

Figure 4.1: Cycling curves of compounds represented by $LiNi_xMn_{1-x}O_4$. At low values of x, a voltage plateau exists at approximately 4.0V. As progressively more Ni is added, a plateau at 4.7V grows. This is the result of Ni cations replacing Mn as the redox-active species. (From Zhong et al.)[44]

Lithium manganese oxide is lithiated according to the following equation:

$$Mn_2^{4+}O_4^{2-} + Li^+ + e^- \rightarrow Li^+Mn_2^{3.5+}O_4^{2-}$$

Oxidation states have been included in order to emphasize the nature of the Li redox reaction. While in the delithiated spinel the Mn is homogeneously in the 4+ oxidation state, upon lithiation half of the manganese accepts an electron and transitions into the 3+ state. The other half of the manganese is not redox active.

By contrast, LNMO is lithiated as follows:

$$Ni_{0.5}^{4+}Mn_{1.5}^{4+}O_4^{2-} + Li^+ + e^- \rightarrow Li^+ Ni_{0.5}^{2+}Mn_{1.5}^{4+}O_4^{2-}$$

Thus in LNMO, all of the Ni transitions by two oxidation states from 4+ to 3+ then from 3+ to 2+, while all of the manganese is inert. This is clearly demonstrated by the composition-dependence of figure 4.1,

in which only ¼ of the Mn must be replaced by Ni in order to fully transition from a Mn-like 4V plateau to Ni-like 4.7V electrochemical behavior. Such a model, by which the 4V plateau is due to Mn and the 4.7V plateau due to Ni redox activity, was directly verified by systematically probing the bandstructure using Ultraviolet Photoelectron Spectroscopy.[45]

b. Order and Disorder

The electrochemical behavior of LNMO is highly dependent on its processing conditions.[46,47] These conditions can be related to atomic structure *via* diffraction data.[48,49] See figure 4.2 for both electron and x-ray diffraction data as a function of lithiation for two different sintering conditions, leading to stoichiometric (low temperature) and slightly off-stoichiometric (high temperature) formulations of the material.

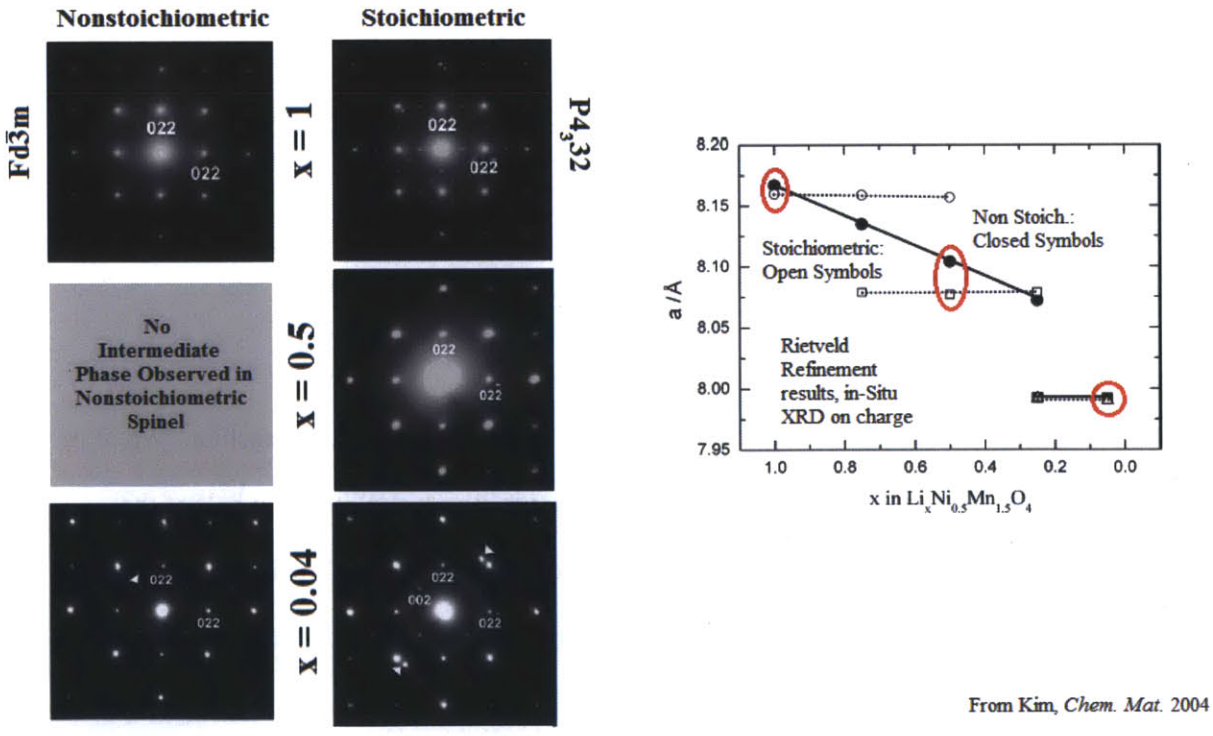

Figure 4.2: Here we have selected area electron diffraction (left) and x-ray diffraction (right) data for LNMO prepared under different sintering conditions and lithiated to different states of charge. The stoichiometric compound is sintered at low temperature (~700C) and slowly cooled, while the nonstoichiometric spinel is sintered at a higher temperature and cooled quickly. x=1 (LNMO) corresponds to a fully discharged battery, while x=0 (NMO) corresponds to a discharged cell. The

material is generally produced as LNMO, and batteries are constructed in the discharged state. (from *Ref. 54*)

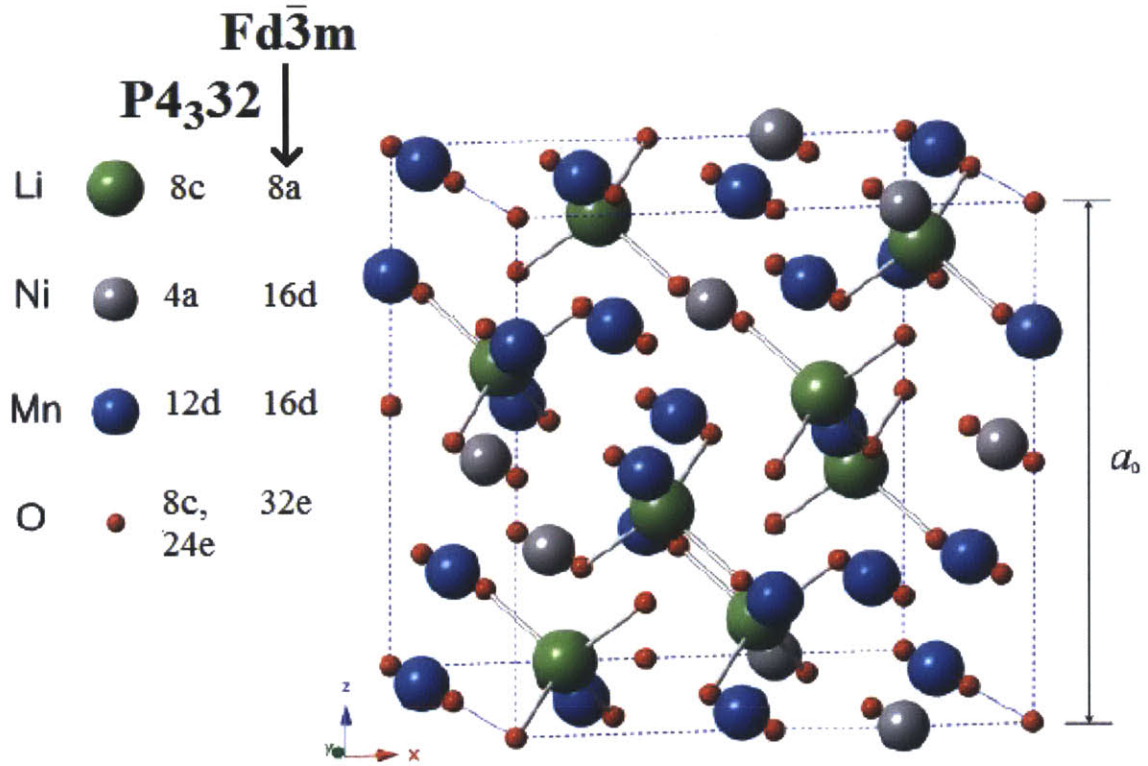

Figure 4.3: This presents the unit cell of LNMO. In the ordered, stoichiometric, polymorph the space group P4332 is observed and Ni and Mn are found at different crystallographic positions. These wycoff positions are 4a and 12d respectively. The disordered spinel has the same bulk structure except that the Ni and Mn are mixed up on the octahedral sites. This causes the material to exhibit the Fd$\bar{3}$m space group, as is common for spinels. In this image the ordered polymorph is shown, but to display the disordered polymorph would be a simple matter of randomly swapping the position of gray (Ni) and blue (Mn) spheres. (Image from 50)

When sintered at ~700C, the spinel is stoichiometric. Both x-ray diffraction and electron diffraction data confirm that this polymorph of the material has the P4332 space group, with an atomic arrangement as shown in figure 4.3. This 'ordered' spinel contains crystallographically distinct positions for the Ni vs. the Mn cations. This produces extra symmetry which is manifest in Selected Area Electron Diffraction (SAED) and in careful X-ray diffraction data by superstructure peaks. These are evident in figure 4.2, as well as in x-ray diffraction data below.

Sintering the spinel causes two separate effects which lead to disorder. One of these two effects, which is thought to occur at temperatures greater than 800C, is a disproportionation reaction:

$$LiNi_{0.5}Mn_{1.5}O_4 \rightarrow qLi_zNi_{1-z}O + rLiNi_{0.5-w}Mn_{1.5+w}O_4 + sO_2$$

This reaction causes Lithium Nickel Oxide rocksalt-structured impurities to precipitate out of the spinel. Such a reaction pulls Ni out of the material, leaving it more manganese-rich than it started, and is tantamount to 'un-doping' the spinel (ie. decreasing x according to the notation in figure 4.1). As would be expected, LNMO treated at high temperatures does indeed show a 4V plateau which is consistent with the decrease in average Mn oxidation state expected as the result of this disproportionation. This can be seen in figure 4.1 and in 4.5.

A second effect contributing to the order/disorder transition was shown by reitveld refinement of neutron-diffraction data. According to the West group, heating LNMO to near 700 °C causes oxygen loss. This formation of $V_O^{\cdot\cdot}$ occurs preferentially at Mn octahedra, causing the reduction of Mn^{4+} to Mn^{3+}, lengthening the Mn-O bonds and increasing the average volume of Mn octahedra. This causes an equalization of the sizes of Mn and Ni octahedra, in a process demonstrated by the data presented in figure 4.4. Once the sizes of the octahedral are equal, Ni hops into the positions originally occupied by Mn. Such a process causes disorder of the metal octahedral. This mechanism is corroborated by a measured inverse correlation between the average oxidation state of Mn and the overall lattice constant of the material in another study.

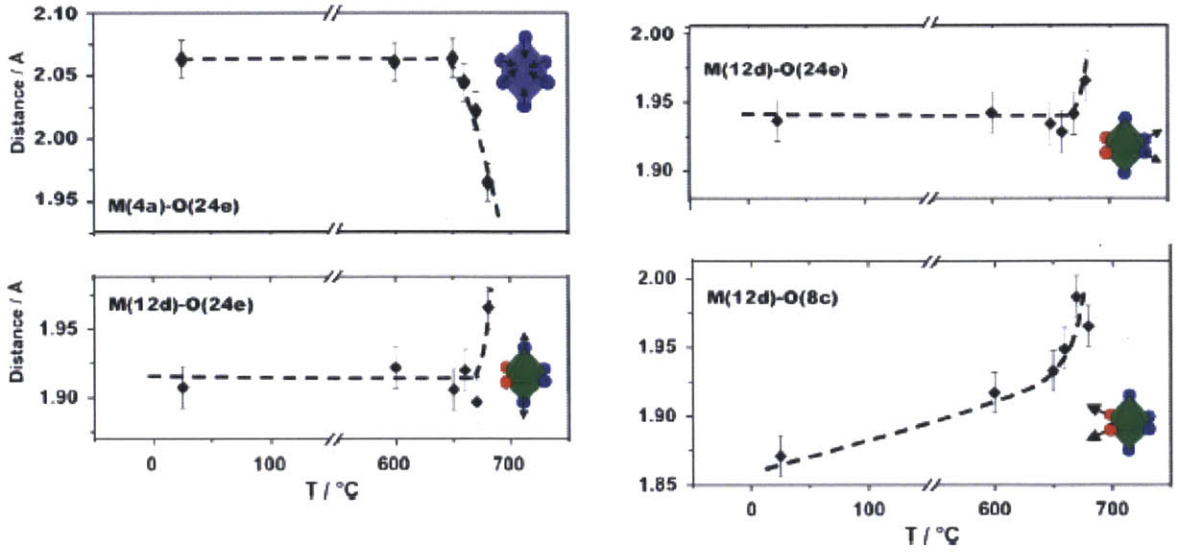

Figure 4.4: These plots show the bond lengths between metal cations in octahedral positions and oxygen atoms in the ordered spinel, calculated based on reitveld refinements on neutron diffraction data. Ni is originally in the 4a site while Mn is in 12d. As shown, upon heating between 650C and 700C the Mn-O bond lengths increase while the Ni octahedral contract. This results in the octahedral sizes equalizing at about 675C. This equalization is thought to promote mixing of cations, transforming the ordered spinel into the disordered. (From reference 51)

It should be noted that both of these mechanisms for introducing disorder into the spinel appear reversible. This can be surmised from the fact that numerous publications initially calcined their material at 900C, a temperature significantly above the order/disorder transition region where both of these effects are observed, but achieved an ordered structure by sintering for an extended period near 700C.

Should the disordered structure be shown to exhibit superior properties, one might seek to achieve a disordered stoichiometric structure to achieve those properties while preserving a 4.7V plateau over the entire range of lithiation. While in principle such a structure may be relatively stable once formed, it might be impossible to achieve due to the fact that oxygen nonstoichiometry appears to stabilize the disordered phase because of the mechanisms discussed above. Furthermore, the distinction between order and disorder must be seen as a difference of degree not of kind. That is to say that a continuum of amounts of disorder exists in this structure, ranging from the perfectly ordered structure to the perfectly mixed (disordered) structure.

c. Effect of order/disorder on structure during cycling

As shown in figure 4.2, XRD data points to significant differences, between the ordered and disordered spinel, in the crystallographic changes induced by (de)lithiation. A primary difference is that the ordered polymorph appears to phase separate twice during cycling resulting in multiple two-phase regions, while the disordered material exists as a solid solution throughout most of the range of lithiation and only phase separates once mostly delithiated. The three phases of the ordered spinel are taken to be a lithium-rich $Li_{1-\delta}\ Ni_{0.5}Mn_{1.5}O_4$ phase, an intermediate $Li_{0.5}\ Ni_{0.5}Mn_{1.5}O_4$ phase with only half of the 8c sites filled, and a lithium-poor $Li_{\delta}\ Ni_{0.5}Mn_{1.5}O_4$ phase.

This interpretation is corroberated by the fact that, as shown in figure 4.2, the disordered spinel lattice constant at these compositions (fully lithiated, half delithiated, and fully delithiated) matches that of the three ordered phases. Such behavior has been independently verified by multiple research groups[46,48,49] and may be a good way to corroborate electrochemical data on the state of delithiation of the spinel.

From these XRD data, it is seen that the ordered spinel exists in a series of two-phase regions for the bulk of the lithiation range sampled in an electrochemical cell. From the arguments presented in IV.i, it may therefore be surmised that the voltage profile is flat. This is indeed the case, as shown in figure 4.5. By contrast, there is no such requirement for the disordered spinel which exists primarily as a solid solution. However, as noted above, such a material may indeed exhibit voltage plateaux in the absence of phase separation if its behavior is dominated by a redox reaction at a single voltage, for example, rather than by the entropic effects governing solid solutions. This is indeed the behavior of the disordered spinel (figure 4.5 a,b), which exhibits two plateaux. These correspond to the $Ni^{4+} \rightarrow Ni^{3+}$ and $Ni^{3+} \rightarrow Ni^{2+}$ reactions.

d. Rate capability of Ordered and Disordered Spinel

Several groups have tested the rate capability of the ordered and disordered spinel and attempted to draw conclusions about the way that order affects transport in the material, and in turn how transport

may affect performance. Figure 4.5 shows one such set of cycling curves from the literature. These data demonstrate ordered spinel with a lower capacity than disordered spinel at the 3C rate. Several research groups have reported similar results.[52,53]

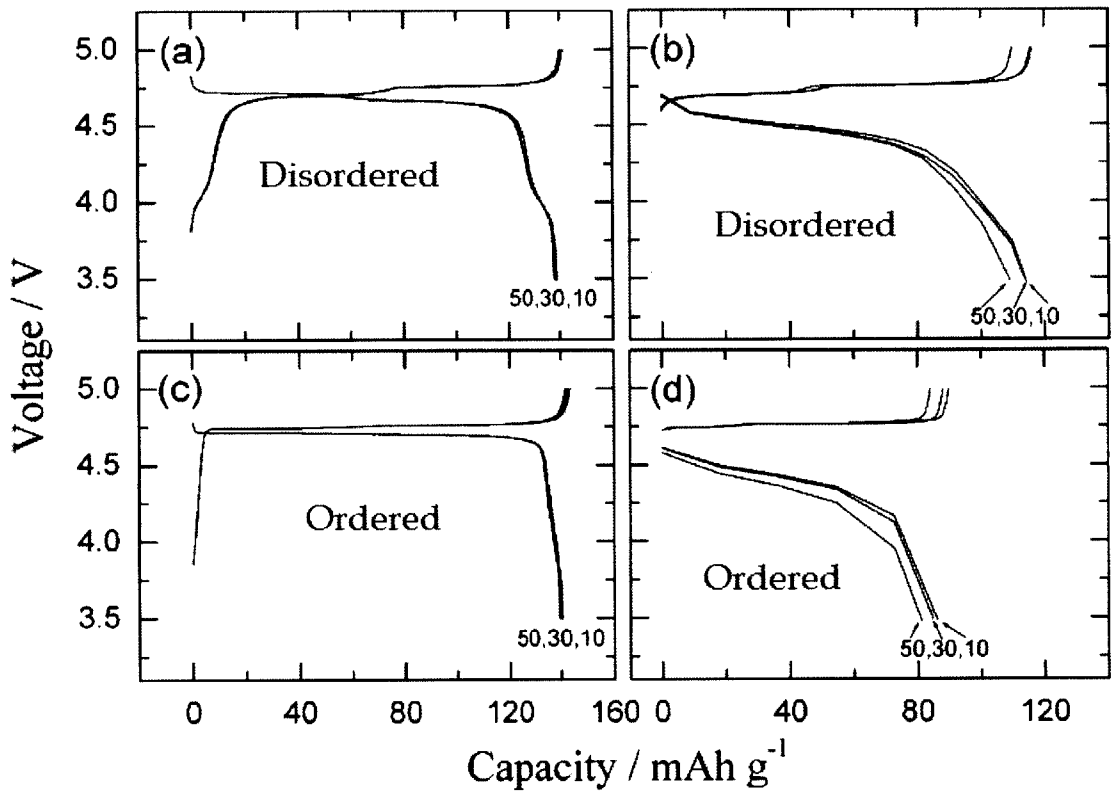

Figure 4.5: A set of cycling curves based on ordered and disordered LNMO spinel (including conductive carbon and binder). The curves in a and c are at the C/7 rate, while the curves in b and d are at 3C. This set of curves demonstrates the main differences reported between the cycling characteristics of the two polymorphs: the constant voltage of the ordered spinel as contrasted to the 4V then ~4.65V and 4.7V plateaux of the disordered, as well as the reported better rate capability of the ordered spinel. The rate capability difference remains controversial. (from reference 54)

The source of the increased rate capability of the disordered spinel is unclear. The Amatucci group increased the carbon loading of electrodes systematically up to 10%, and observed an increase in rate capability. Beyond 10% carbon loading, the group claims that the ordered and disordered spinel exhibited similar capacities. This was taken as evidence that the higher electronic conductivity measured in the disordered spinel causes the material to have a higher rate capability.

However, it has been pointed out as well that the mixture of Mn3+/Mn4+ is likely the source of higher rate capability of the disordered spinel (as compared to the ordered, in which all Mn is in the 4+ state). The material exhibits a 4V plateau upon delithiation before the 4.7 volt plateau begins. Along this plateau the Mn3+ is presumed to be oxidized to Mn4+, which indicates that early on in cycling the higher conductivity of the disordered spinel ought to disappear. However, as no one has as yet published conductivity data as a function of charge state, this has not been confirmed.

Furthermore, in the same paper as in which the above objection was raised, ordered LNMO with significant rate capability at 40C was demonstrated.[55] This proves that the material is capable of significantly higher rates than those observed in the initial comparative studies.

It should be pointed out that the difference in phase separation behavior may play a role in any observed difference in rate capability. The effect of phase separation on the kinetics of Li intercalation is demonstrated in Galvanostatic Intermittent Titration (GITT) measurements in figure 4.6. This measurement technique is based on the voltage evolution of a composite cathode, held at constant current. The voltage profile is fit to Sand's equation, which is based on a model that does not account for phase separation.[56] Similarly, Potentiostatic Intermittent Titration may be used to measure diffusivity, which is fit to the Cottrell equation and likewise does not account for phase separation. While versions of GITT have been reformulated to deal with phase separated cathodes,[57] no mention of an effort to account for phase separation was made in literature measuring diffusivity of LNMO[62, 67, 43] as far as the author is aware. Furthermore, attempting to measured diffusivity via GITT within a phase-separated region is known to result in erroneous[58] and low[59] diffusivity values for a range of cathode materials. Together, this suggests that the apparent depressed diffusivity measured in a two-phase region – while not the true diffusivity of the bulk material – may represent measurably detrimental effects of phase boundary motion on Li-insertion kinetics. Thus, phase boundaries may result in sluggish cycling kinetics and thereby decrease the cycle rate of the ordered spinel (multiple phase transformations) compared to the disordered (single phase transformation).

Furthermore according to recent work modeling phase separation kinetics in intercalation materials it is possible that phase separation occurs at low and intermediate cycle rates only, and does not have time to occur if the material is rapidly lithiated.[60,61] This may resolve any contradiction between phase separation slowing Li insertion kinetics in the disordered spinel with the observation of 40C cycling in the ordered polymorph.

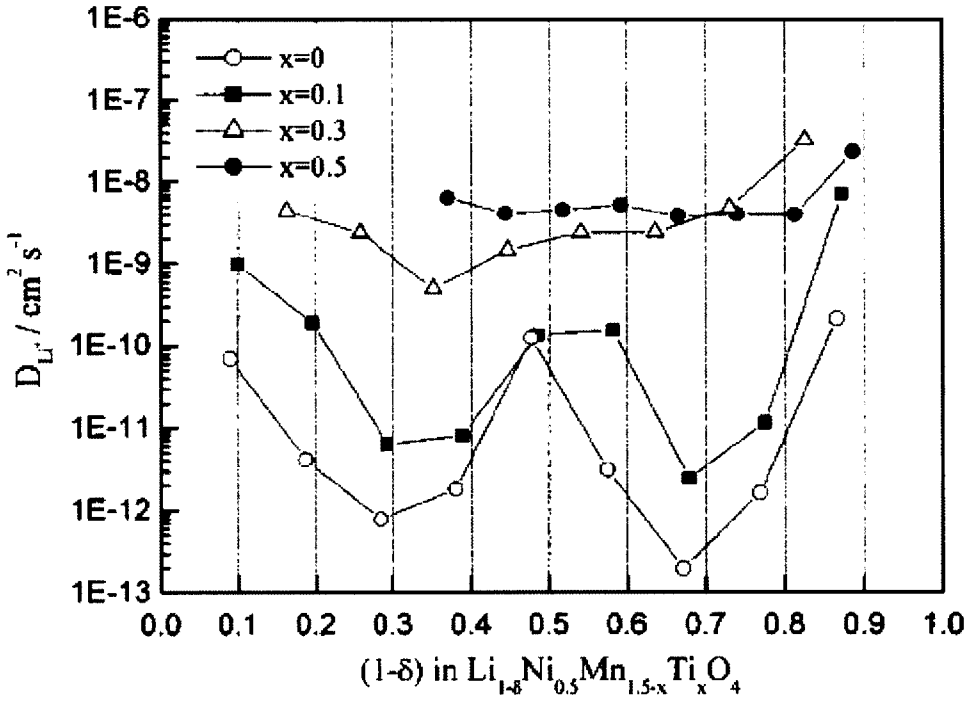

Figure 4.6: This plot gives chemical diffusivity, measured by GITT, of LNMO doped with different levels of Ti. As shown, the undoped ordered spinel (x=0) has two diffusivity minima at the 30% and 70% delithiated states. These correspond to phase separated regions. Upon doping with Ti, these minima disappear. Doping is independently in this study confirmed to suppress phase separation. This therefore constitutes indirect evidence that phase separation may cause a slowing of Li insertion kinetics (from reference 62)

Appendix A presents a first-order estimate of the voltage drops resulting from ionic and electronic transport in battery cathodes. According to this analysis, for a conventional electrode (ie. including binder and conductive additive) of standard thickness the primary source of resistance ought to be due to ionic current through the electrode pores. This would suggest that neither electronic conductivity nor ionic diffusion in the active material plays a rate-limiting roll.

Ultimately, rate capability is strongly dependent on cell design. This was demonstrated recently by making a nanostructured LMO cathode with >100 mAh/g capacity at 743C.[63] Such 'ultrafast discharge' supports the idea that, regardless of the rate capability measured in conventional electrodes, it is important to have good data regarding electronic and ionic transport in active materials to enable us to design future batteries which take full advantage of the properties of their electrode materials. The current study seeks to contribute to this aim.

e. Effect of doping

A literature review of progress in LNMO must include data regarding attempts to dope the material with alternate metal ions. LNMO has been doped with Ti, Fe, Mg, Fe, Co, Cr, Ru, V, and Cu.[64],[65],[66] One of the effects of most interest is that Fe, Ti, Co stabilize the disordered phase. First-principles studies suggest that Co and Cu doping can improve Li diffusion.[67] Fe appears to migrate to the surface of LNMO particles during cycling and simultaneously improve charge transfer kinetics while suppressing the formation of a thick SEI.[68] Ru appears to improve the rate capability and cycle life of LNMO, allowing the cathode after 500 cycles to exhibit 91% of its nominal capacity after 500 cycles.[69]

V. METHODS EMPLOYED

a. Electrode Design

The electrodes generally studied in electrochemical research into battery active materials are based on the electrode compositions used in industry. These include three components: a binder (generally an electrochemically inert polymer such as PVDF or PTFE), the active material, and a conductive additive. This mixture is often coated onto an aluminum current collector.

Such electrodes are conductive and allow easy electrochemical delithiation. They may be readily used for XRD studies looking at the phase change behavior of LNMO since the XRD signal from graphite may be readily removed or ignored. However, such electrodes would not work for electronic conductivity studies since the conductivity of the total electrode would be too heavily influenced by the conductive additive. In order to measure the electronic conductivity of the active material, I thus used additive-free sintered LNMO pellets. Starting with powder supplied by NEI, I pressed the material into pellets and sintered them. I then polished these pellets and coated one side with graphite as a conductive additive, using the result as a positive electrode for delithiation.

b. Sintering Conditions

There is a significant amount of literature on the sintering conditions used to make ordered and disordered LNMO. My goal was to make several samples of both polymorphs, then to examine differences in the electronic conductivities of these polymorphs. Beginning with values from the literature, I thus explored several different sintering conditions in my electrode fabrication. The main variables found to influence the properties of the final pellet were sinter temperature, sinter time, and cool rate.

After sintering, the samples' porosities were measured using the Archimedes technique. In this technique, three four-point probe mass measurements are taken: the dry sample weight, submerged sample weight in isopropanol, and wet sample weight. On the assumption that the fluid fills all the open

pores, these three measurements are used to calculate the sample's open porosity, closed porosity, and solid volume fraction (with these three measurements adding to 1).

c. X-Ray Diffraction

X-Ray Diffraction (XRD) was the primary method I used to verify the purity of my sintered samples, distinguish between ordered and disordered LNMO, and to characterize phase transition behavior and lattice constant evolution during lithiation. Crucially, it is possible with a slow XRD scan to view superstructure peaks in the ordered spinel and thereby to distinguish it from the disordered polymorph.

The phase behavior of ordered and disordered LNMO, having been studied in the literature (see figure 4.2, above) was used as a method of verification of the amount of delithiation of my samples. This was particularly useful as the likelihood of electrolyte decomposition at high voltage is impossible to distinguish based on voltage curves from sample delithiation. As a result, electrochemical measurements of the amount of delithiation of my samples were taken to be less accurate than inferences based on XRD.

d. Electrochemical Delithiation

After sintering ordered and disordered samples, cells were constructed to both delithiate additive-free samples for conductivity measurements as well as to cycle conventional cells to electrochemically asses the amount of Mn^{3+} produced during sintering. While the additive-free sintered samples used to evaluate electrical conductivity were simply made of polished sintered pellets, voltage curves were also collected using conventional cells. The method employed was based on reference #55. The electrodes consisted of 80 wt% LNMO, 15 wt% Super P conductive carbon, and 5 wt% PTFE.

All electrodes were loaded into Swagelok cells (see image 5.1). These were used as a standardized cell casing in order to delithiate samples in a controlled fashion. Cells were assembled in a glovebox, and used Li foil as an anode. 3 pieces of Celgard separator were used, along with 1M LiPF6 in 1:1 (by volume) EC:DEC as electrolyte.

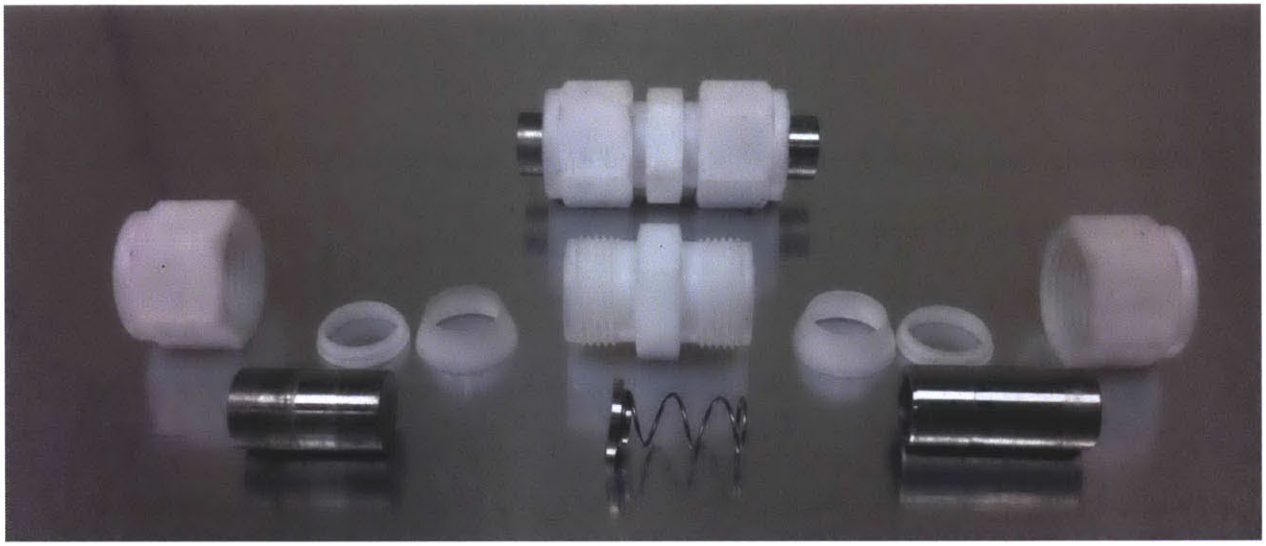

Figure 5.1: Cells were constructed using Swagelok casings. An assembled cell is shown at the top, while the dis-assembled parts are found in the lower part of the image. Metal parts are composed of stainless steel, while the remainder of the casing is made of Teflon.

Several C-rates were attempted with the sintered samples, ranging C/20 to C/300. It was only at very low rates that the sintered samples maintained structural stability during delithiation and could subsequently be removed from the cell with limited amounts of fracture. Conductivity tests (see Chapter VI) were thus done using the C/300 rate for delithiation. While such a low rate made the tests possible, undesireable effects such as side reaction and self-discharge became more prevalent in these tests than they would have been at higher rates. It is also thought that some cells grew dendrites which penetrated the separator and contributed to self-discharge. As a result of these effects, the lithiation ranges achieved in these tests involved a lower range of states than the range targeted. For results, see Chapter VI below.

e. VAN DER PAUW

Van Der Pauw measurements constitute a four-probe conductivity measurement technique. Measurements are made on a flat, thin, singly connected sample of uniform thickness but arbitrary shape (see image 5.2). Four points – A, B, C, and D – are defined near the edge of the sample, and a current is passed through two of them while the voltage is measured across the other two. The ratio of these measurements is defined as a resistance:

$$R_{ABCD} = \frac{I_{AB}}{V_{CD}}$$

Two measurements are taken this way, R_{ABCD} and R_{BCDA}. It can be shown[70] that the sample resistivity must satisfy the equation:

$$1 = e^{\frac{-\pi d R_{ABCD}}{\rho}} + e^{\frac{-\pi d R_{BCDA}}{\rho}}$$

Where d is the sample thickness and ρ is the sample resistivity. A benefit to a four-point probe experiment as compared to a two-point probe is that contact resistances will not affect the overall measurement. Figure 5.3 shows an error analysis on a VanDerPauw system. Finite element analysis was used to simulate the VanDerPauw result and compare to the actual conductivity of the simulated material. Error was evaluated as a function of sample thickness and contact size. Given a contact size, this study provides an estimate of VanDerPauw error.

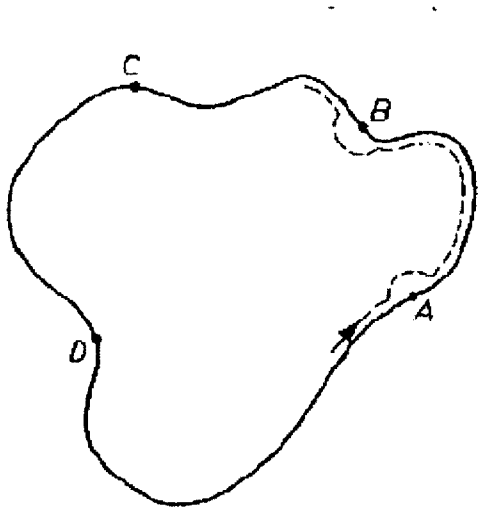

Figure 5.2: VanDerPauw sample geometry. Points A, B, C, D must be near the perimeter of the sample and be small. Sample must be thin and singly connected. From *Reference 70.*

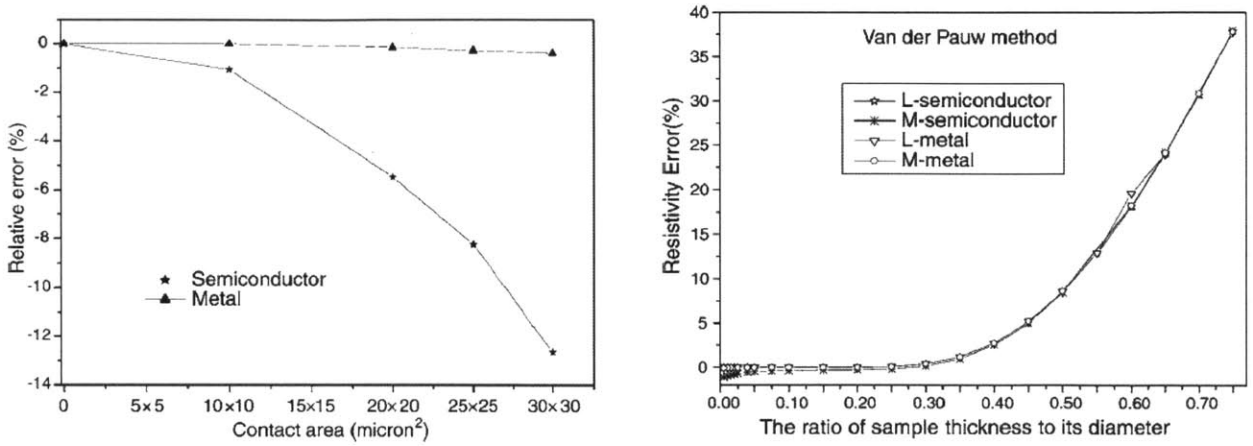

Figure 5.3: Results of error analysis on simulated VanDerPauw sample. Sample was a 200um diameter disk. Effect of sample thickness and contact size on semiconductor and metallic samples was evaluated based on numerical finite element simulation. From *Reference 71.*

For the present study, samples were removed from cells following delithiation in Ar glovebox and washed 3 times in Diethyl Carbonate (DEC). Samples were allowed to soak overnight in DEC, then washed 3 times with isopropanol. Samples were dried and both sides were polised to remove graphite conductive coating and any residual Li salts. Contacts were painted on with silver paste, then heated to 110°C in a glovebox. Following this, temperature-dependent VanDerPauw measurements were performed in glovebox using custom-built four-point probe setup.

Probe setup was constructed to include four commercial probes on an insulating sample stage. Thermoelectrics built in to the stage were used to control temperature. A thermocouple attached to the stage (Omega) was used to measure the temperature. A cell cycler (BioLogic) was used to perform the VanDerPauw measurements.

See Appendix B for more details on experimental procedure.

Figure 5.4: Custom-built four-point probe setup used to measure sample conductivities.

VI. CONDUCTIVITY AS A FUNCTION OF LITHIATION STATE

a. Sintering conditions for ordered and disordered LNMO

Three sintering conditions were explored. One was based directly on the literature, and was used to make ordered LNMO. Two more conditions were tried, raising the temperature to result in increased disorder. Furnace cool refers to simply switching off the furnace at the prescribed time and allowing it to cool on its own. The most disordered sample was made by sintering at 800C for only 24h and cooling in a controlled manner.

Batch	Sintering #1	Sintering #2	Cooling
Ordered (Based on Ref. 55)	900C, 18h	700C, 48h	1°C/min
Disordered #1	900C, 18h	750C, 48h	Furnace Cool (fast)
Disordered #2	900C, 12h	800C, 24h	9°C/min

Table 6.1 displays the sintering conditions developed for the samples used in this study.

Figures 6.1 and 6.2 present x-ray diffraction data for the ordered and disordered samples. A Reitveld Refinement of the ordered sample shows superstructure peaks and suggests that any impurity is less than 1 wt% of the total sample. The disordered spinel shows no superstructure peaks, as expected.

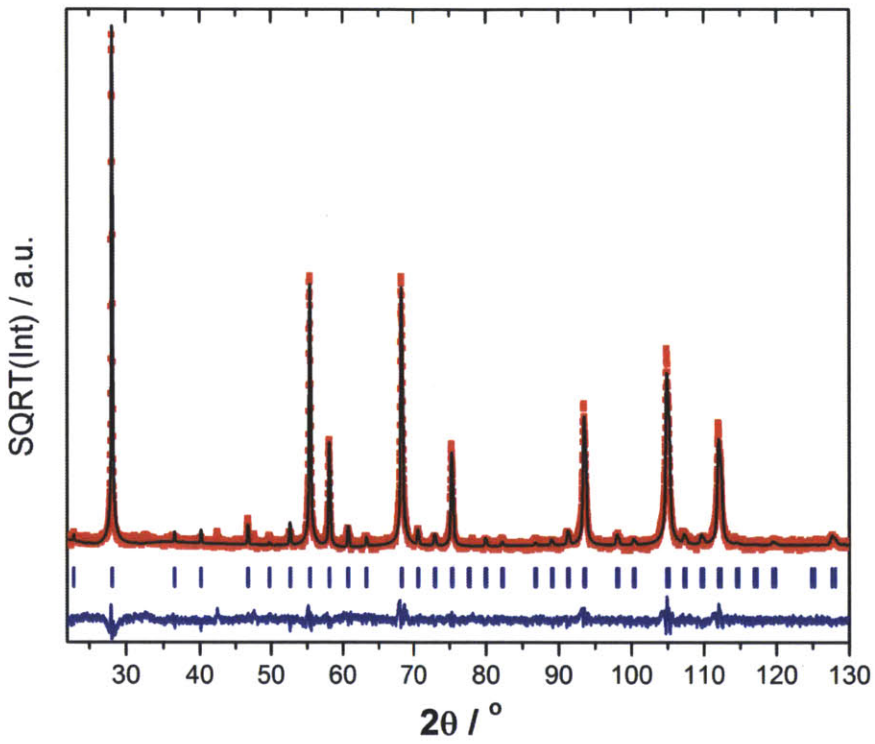

Figure 6.1: XRD scan of ordered spinel, using Cr source. Refinement done by Dorthe Bomholdt Ravnsbaek. Lattice constant found to be 8.169Å, which is in good agreement with literature data (see figure 4.2). Superstructure peaks are clearly visible. RBragg = 6.45%.

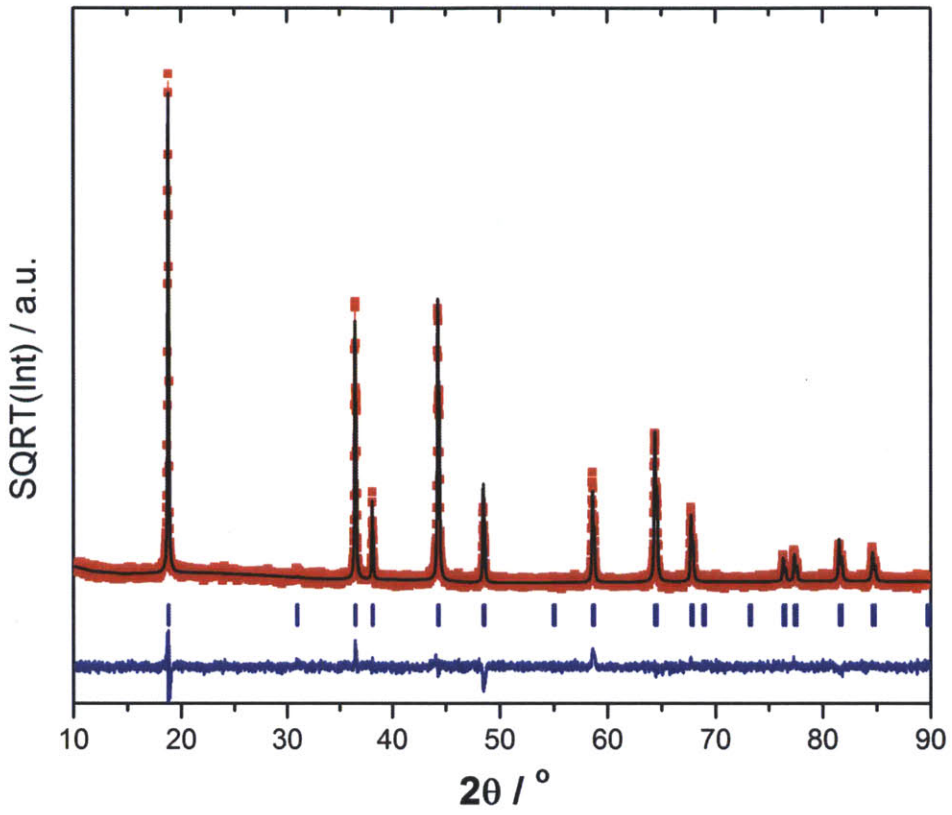

Figure 6.2: XRD scan of fully lithiated disordered spinel, using Cu source. Refinement done by Dorthe Bomholdt Ravnsbaek. Lattice constant found to be 8.175Å, which is in good agreement with the literature (see figure 4.2). No superstructure peaks visible. RBragg = 5.68%

SEM images were taken of both ordered and disordered samples (see figures 6.3 and 6.4). Morphologies of the two samples appeared similar, as expected because both were initially sintered at 900C. Both samples exhibited a larger than expected variation in crystallite size, with grains ranging from about 0.5 um to about 5 um.

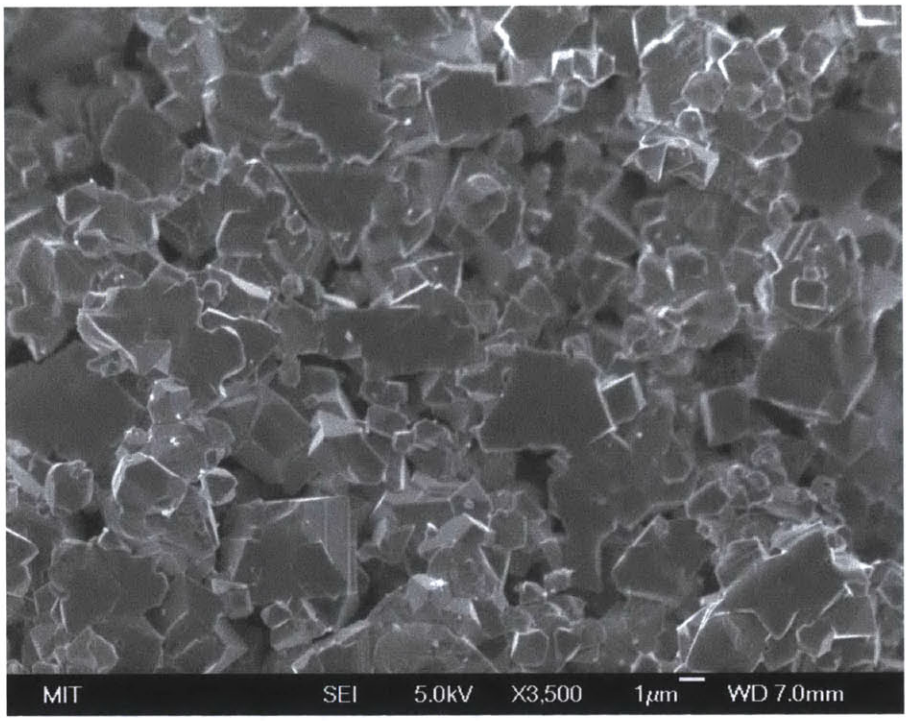

Figure 6.3: Morphology of the ordered spinel, sintered at 900C for 18h then at 700C for 48h. Cooled at 1C/min. Large variation in grain size is observed.

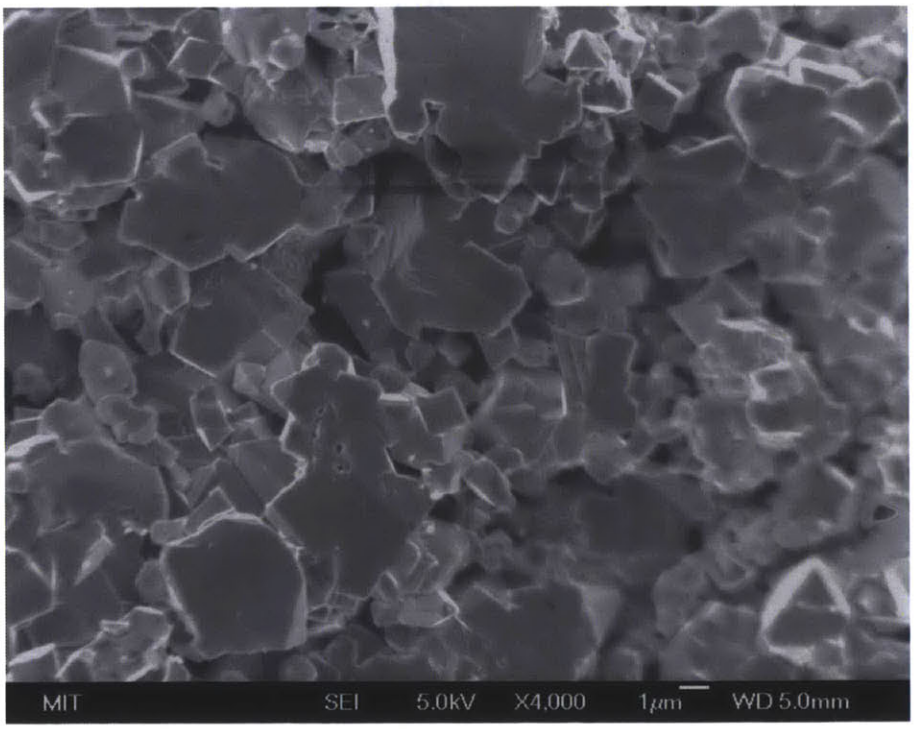

Figure 6.4: Morphology of the disordered spinel, sintered at 900C for 18h then at 750C for 48h. Furnace cooled. Large variation in grain size is observed.

b. Van Der Pauw Control tests

Before performing conductivity measurements as a function of lithiation state, it was necessary to perform control tests to verify the methods used. Particularly, verification was needed that:

1. Samples could be fabricated so that sample-to sample variation was low
2. LNMO was stable under the conditions being measured
3. The process of coating one surface of the electrode with conductive carbon, inserting the electrode into a cell, drying, and polishing off the carbon did not affect measured conductivity.

Figure 6.5 shows three sets of conductivity data taken for a disordered sample, sintered at 800C. Two samples were used. The datasets marked 'pristine' in the legend were measured as sintered. The third dataset was for a cathode that was put into a cell but not delithiated; it was simply removed after one day, washed, and measured. As one can see from these data, measured conductivity values were consistent across datasets with minor differences in the activation energy. These three datasets thus show that the sample-to-sample variation can be made low, that LNMO appears stable with temperature cycling, and that exposure to the interior of a cell does not affect measured conductivity.

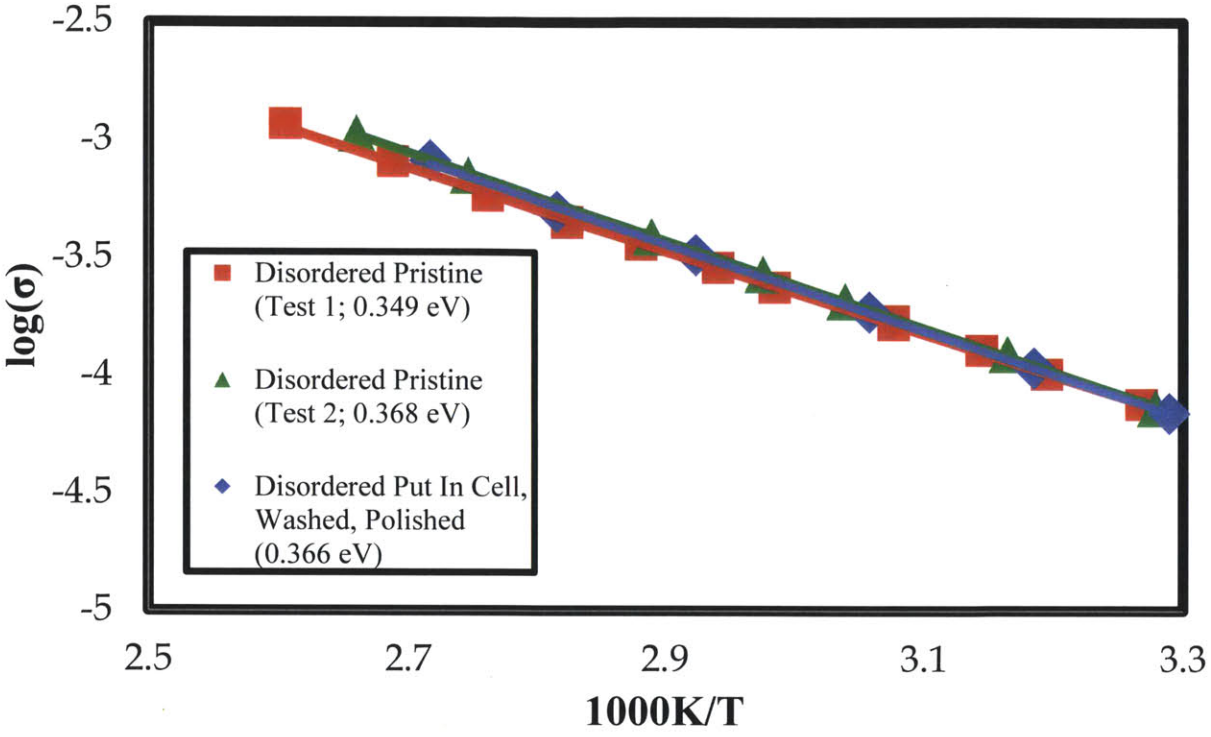

Figure 6.5: Van Der Pauw control tests. These are conductivity data of two samples, both sintered at 800C. Activation energies calculated based on slopes of best fit lines.

c. Conductivity of Fully Lithiated Spinel and Sintering conditions

Next, the conductivities of the three as-sintered spinels were measured and compared to the values in the literature. For literature values see figure 6.6, for conductivities as measured in this work see figure 6.7.

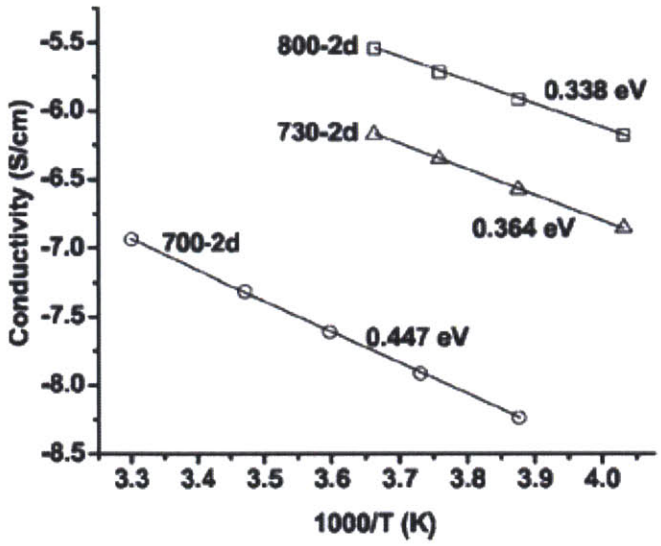

Figure 6.6: Low-temperature arrhenius diagrams from the literature of fully lithiated LNMO. Sintering conditions and activation energies are written on plot next to the lines representing them (From *Reference 72*)

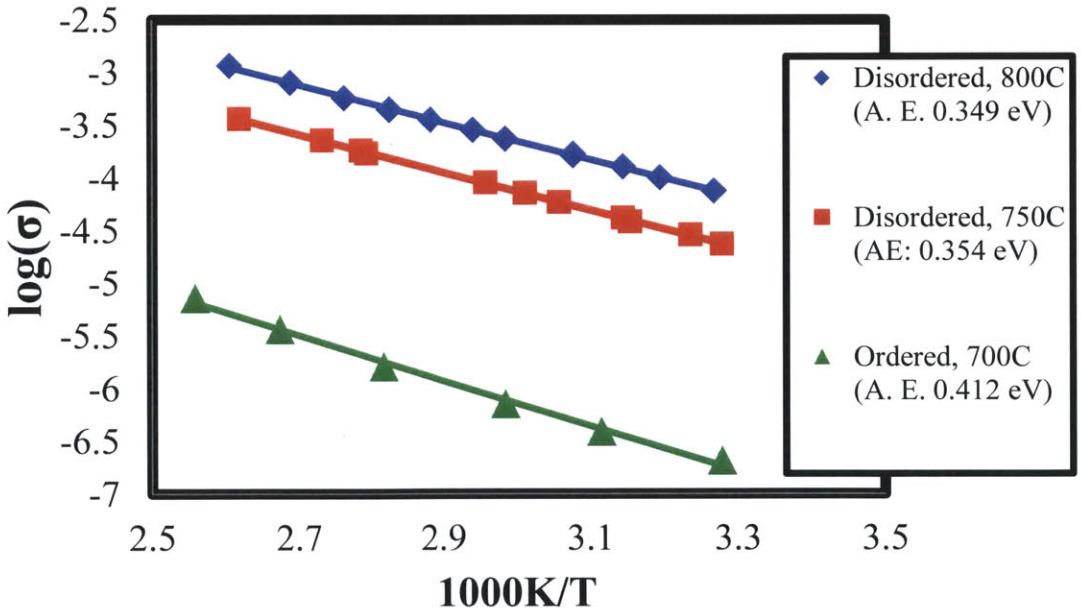

Figure 6.7: Arrhenius diagrams from measurements of LNMO under different sintering conditions.

As seen from comparing figures 6.5 and 6.6, these measurements display the same trend in conductivity value and activation energy as that displayed in the literature. The ordered spinel gives about the same conductivity and a similar activation energy. As sintering temperature increases,

conductivity increases and activation energy decreases. The literature dataset for the sample treated at 730°C is about an order of magnitude less conductive than the sample measured here which is treated at 750°C, following the overall trend of higher sintering temperatures leading to greater conductivity values. This is likely because such samples exhibit a greater degree of disorder, and so the product $[Mn^{3+}][Mn^{4+}]$ is higher.

d. **Ordered spinel conductivity as a function of lithiation**

Several samples were made of the ordered spinel and systematically delithiated by different amounts at the slow C/300 rate. The samples were removed from their cells and both XRD and Van Der Pauw measurements were taken. All of these steps followed the procedures outlined in Appendix B.

XRD scans are shown in figures 6.8 and 6.9. Table 5.2 summarizes the results of analyzing these data.

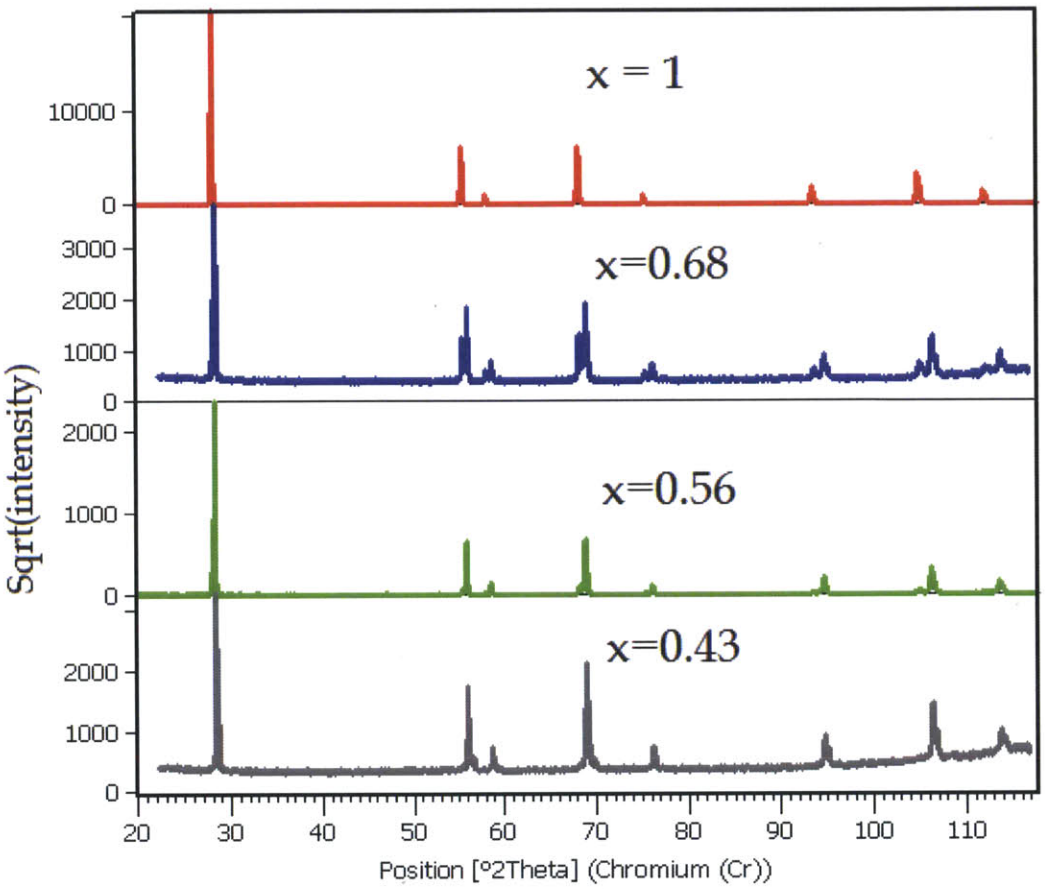

Figure 6.8: XRD profiles of ordered samples delithiated to different charge states. The parameter x refers to the chemical formula $Li_xNi_{0.5}Mn_{1.5}O_4$ and was calculated based on the lattice constants and weight fractions induced from these scans. Differences in data quality are largely due to the sizes of the samples. Partially delithiated samples tended to crack upon removal from the cell, causing the end sample to be smaller and the signal to noise ratio to be worse.

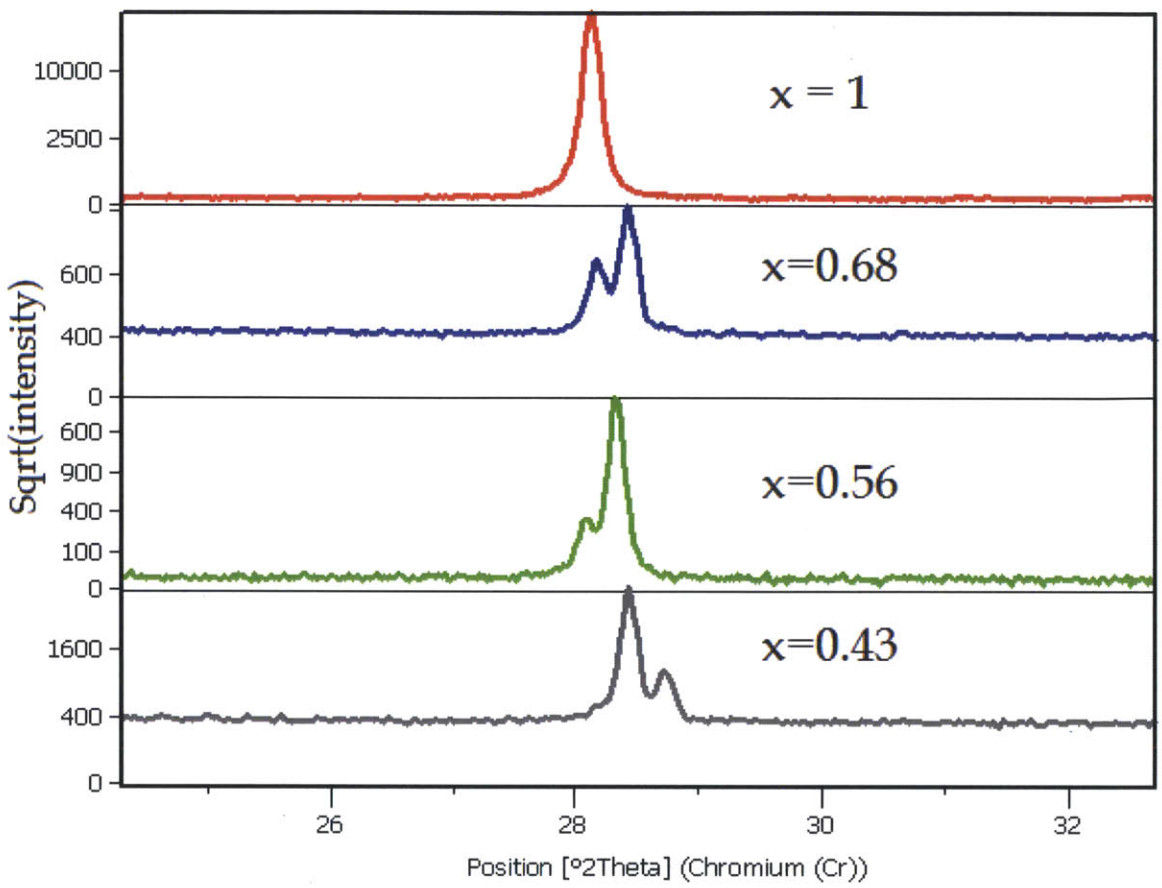

Figure 6.9: A view of the same data as in figure 6.8, but focused on one peak only. The parameter x refers to the chemical formula $Li_xNi_{0.5}Mn_{1.5}O_4$. The graphs demonstrate the three-phase behavior observed in the ordered spinel as it is delithiated. Reitveld analysis confirms that the x=0.68 and x=0.56 samples suffered from a small amount of mis-alignment, causing the peaks to be shifted slightly. These samples were both small, having been badly broken upon being removed from their Swagelok cells, which made them difficult to polish and align perfectly.

x in $Li_xNi_{0.5}Mn_{1.5}O_4$	Phase I x = 1	Phase II x = 0.5	Phase III x = 0	% Side Reaction
x = 1	8.169Å +/- 0.001Å (99 wt%)	-	-	-
x = 0.68	8.16Å +/- 0.01Å (33 wt%)	8.08 Å +/- 0.01Å (67 wt%)	-	0.3% (within error)
x = 0.56	8.17 Å +/- 0.01Å (10 wt%)	8.10 Å +/- 0.01Å (90 wt%)	-	44.5%
x = 0.43	-	8.088 Å +/- 0.001Å (87 wt%)	8.005 Å +/- 0.001Å (13 wt%)	28.3%

Table 6.2: presents results of Rietveld analysis on samples of ordered LNMO. The lattice constants of the first two phases agree with the results given in the literature, which are approximately **Phase I: 8.16Å, Phase II: 8.08Å, and Phase III: 7.99Å** (from figure 4.2 and *Ref. 54*). While the differences between the data presented here and those in the literature are not within experimental error, slight differences in processing conditions can easily explain this. Lithiation state is calculated from phase composition, assuming that the three phases are respectively fully, half, and completely de- lithiated. The % Side Reaction is derived from comparing this XRD-derived value of delithiation to electrochemical data. It represents the fraction of current which went through the Swagelok cell which did not contribute to delithiation of the cathode.

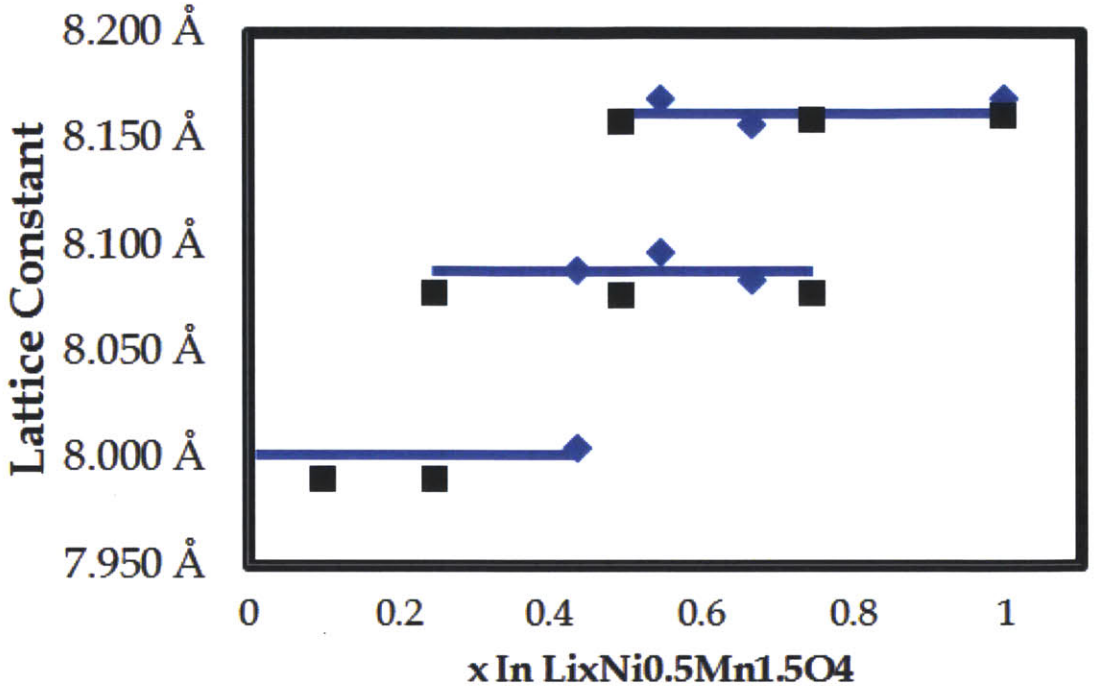

Figure 6.10: plots for the ordered spinel, the lattice constant of each phase determined from a rietveld refinement of the XRD data (blue diamonds) along with literature data (black squares, from *Ref. 54*). Horizontal blue lines represent the approximate lattice constant and composition range of those phases deduced from these data.

Several conclusions may be drawn from the XRD data. The first is that the phase separation behavior of the ordered sample appears to be supported in this data as three phases are observed. Figure 6.10 compares the Rietveld analysis results to literature data. In the ordered spinel, it is apparent that small amounts of delithiation cause phase separation to take place between lithium-rich and lithium-poor regions of material. Three phases in total were observed. The degree of lithiation was calculated based on the relative mass fractions (determined from peak intensities in the XRD data) of these phases, assuming that these phases correspond to x=1, x=0.5 and x=0 as stated in the literature.[54, 48]

A second phenomenon demonstrated by the XRD data is that progressively more delithiated samples yield lower quality XRD data on average. This is due to the structural stability of the additive-free sintered samples becoming progressively undermined as the samples were further delithiated, making them more likely to break into smaller pieces when they are removed from the cell and polished for

measurements. These smaller pieces were more likely to be rough, and difficult to align in a goniometer. This problem was not observed in the literature, as literature tests employed conventional electrode composites. The structural stability of such electrodes is derived from an inert binder (usually an organic compound) and is thus not affected by delithiation. Clearly, however, such samples would not have worked for conductivity measurements of LNMO as they employ a conductive matrix.

A third conclusion from the XRD data is that electrochemical delithiation is not an accurate way of gauging the charge state of these electrodes for highly delithiated samples. The final two samples were delithiated to approximately x=0.4 and x=0.2 respectively, according to the electrochemical measurement. However, the XRD data shows that these samples were actually only delithiated to x=.68 and x=.43 respectively. This indicates that a significant fraction (45% and 28%, for these two samples) of the current being passed through the cell fueled side reaction rather than delithiation or was lost to self-discharge. It was thus difficult to predict the actual lithiation state of a sample from electrochemical data alone, and the samples produced did not represent as wide a range of lithiation states as originally planned.

Likely, for higher currents the 'delithiation efficiency' would have been higher as the side reaction current would have represented a lower fraction of the total. The samples used were delithiated at C/300. When higher currents were attempted the samples generally broke upon being removed from the cell. This is likely due to sharper gradients in lithium content derived from rapid charge transport leading to vegard strain causing high stresses in the material, resulting in electrochemical shock and cracks in the microstructure. A very slow C/300 rate was thus chosen to maintain sample integrity.

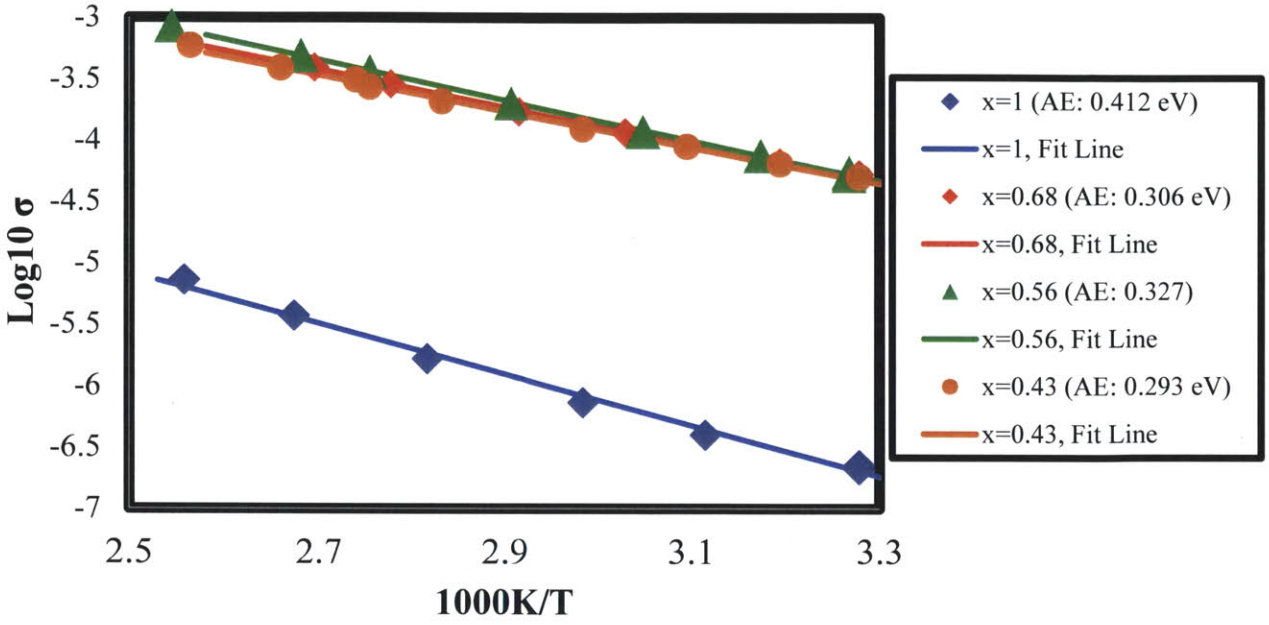

Figure 6.11: Conductivity of ordered samples at various states of delithiation. This demonstrates trends associated with the electrochemistry of the material.

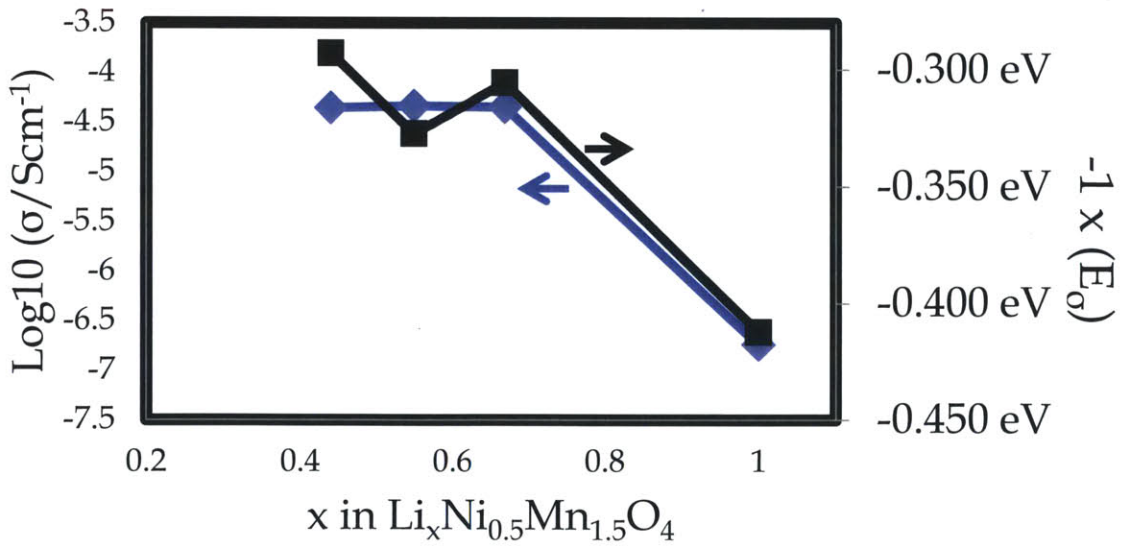

Figure 6.12: demonstrates the relationship between conductivity at 30°C and activation energy in the ordered spinel, as a function of lithiation. It appears that a change in activation energy with lithiation state largely explains the change in conductivity observed.

Figure 6.11 shows the conductivities measured for the ordered samples. This plot shows that conductivity is lowest for the fully lithiated sample, and increases as the spinel is delithiated. Arrhenius data were fit to a line. In all cases the R^2 value of this line was greater than 0.99, indicating that the data

collected were very linear (with the ideal value being 1). Conductivity values at 30°C were calculated from the equation of this line, as the precise value of the nearest temperature to 30°C actually measured varied by several degrees.

In order to determine the origin of conductivity changes, the activation energy of each dataset was calculated from the following equation:

$$E_\sigma = -\frac{d[\log(\sigma)]}{d[1/T]}\,k$$

In this equation, derived from the Arrhenius relation, k represents Boltzmann's constant. In order to see what effects a change in activation energy may have on measured conductivity, one may look at the Arrhenius relation:

$$\sigma \sim e^{\frac{-E_\sigma}{kT}}$$

$$\Delta\, log(\sigma) \sim -\Delta E_\sigma$$

Thus, the activation energy is plotted along with the logarithm of the conductivity in figure 6.12. It appears from these data that changes in log(σ) are, on average, proportional to corresponding changes in activation energy. Changes in this activation energy thus appear to explain, largely, the differences in conductivity observed as a function of charge state.

To interpret the activation energy requires more thought. In general, for a semiconductor, it may be seen as:

$$E_\sigma = E_\mu + E_A$$

In which E_A corresponds to the energy of carrier generation – ie. the bandgap of the material – and E_μ represents carrier mobility (or hopping energy in the small polaron model). As carrier concentrations have not been measured directly, we cannot directly determine the relative weights of these two effects. However, we may draw some conclusions from these results in light of the recent bandstructure

calculations presented in figure 6.13. These indicate that the bandgap of ordered LNMO is greater than 1eV. That value is significantly higher than the activation energies E_σ measured here, indicating that thermal generation of carriers is likely not a factor in the observed Arrhenius behavior. This result suggests that $E_\sigma = E_\mu$, and that the Arrhenius increase in conductivity is due to easier thermally activated electron hopping at high temperatures; ie. to an increase in polaron mobility. These activation energies are in a reasonable range for such an interpretation to be valid, in light of previously measured electron hopping energies measured in oxides exhibiting the small polaron conduction mechanism (see table 3.1).

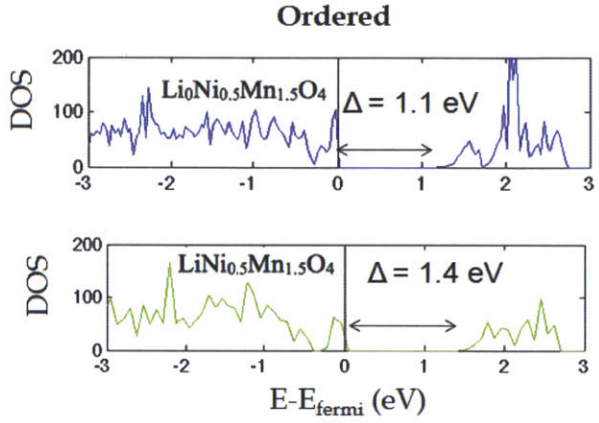

Figure 6.13: Bandstructure calculations on lithiated and delithiated, ordered LNMO. These calculations show a bandgap that is significantly wider than the E_σ measured in the current work. This indicates that the observed activation energy corresponds to electron mobility rather than carrier formation. The ordered spinel is likely to exhibit fewer thermally induced carriers and will act as an extrinsic semiconductor with the carrier concentration determined primarily by composition. (From *Ref 19*)

This conclusion – namely that electron mobility and not thermal carrier generation dominates conductivity under standard conditions - indicates that the concentration of carriers in the material is dominated by sample composition as in an extrinsic semiconductor. This composition will be highly dependent on lithiation state and will vary markedly between ordered and disordered polymorphs of LNMO. This analysis is continued below in section II.vi.

e. Disordered spinel conductivity as a function of lithiation

Disordered samples were delithiated to varying charge states and measured, using the same procedure as for the ordered samples. Figure 6.14 and 6.15 show XRD scans from these samples, the peaks of which were observed to shift to higher values with increasing electrochemical delithiation. Table 6.3 summarizes the results of Rietveld refinements on these data.

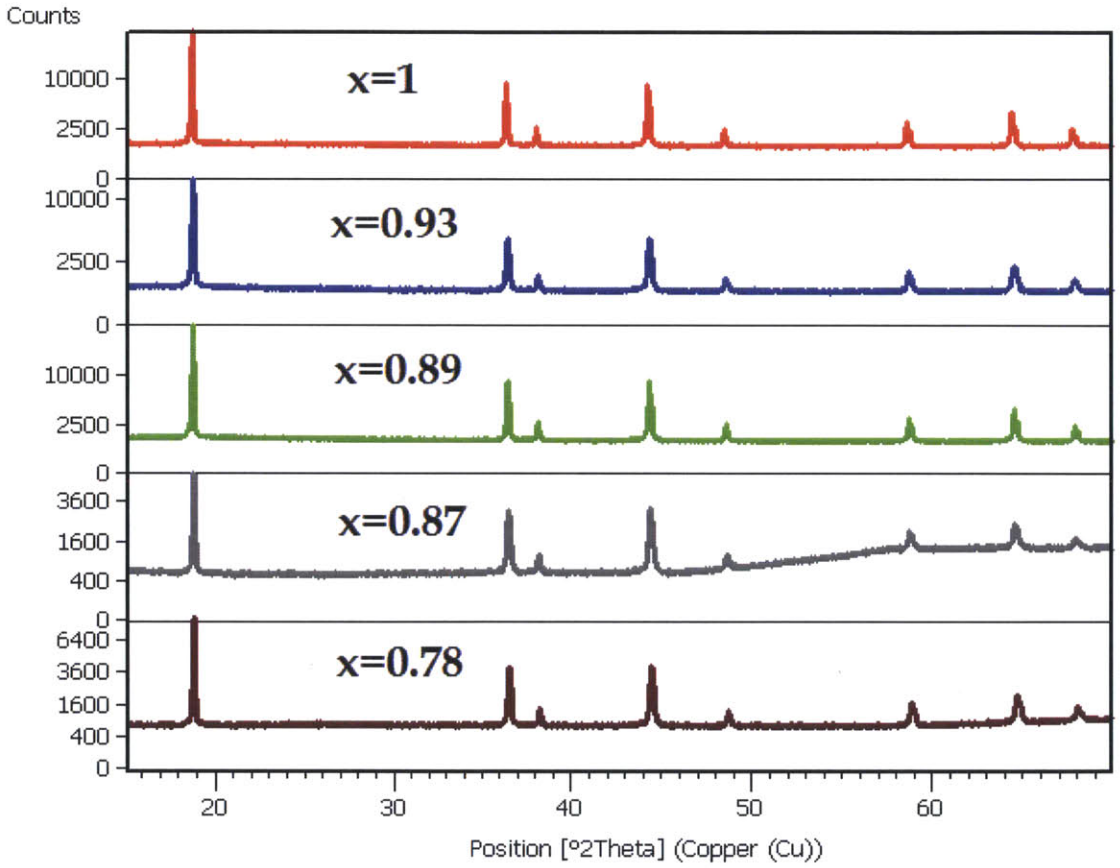

Figure 6.14: XRD profiles of disordered samples delithiated to different charge states. The data quality becomes worse for higher charge states, which is largely the result of smaller samples resulting from the increased brittleness of delithiated sintered pellets. These smaller samples are more difficult to align and do not cover the entire x-ray beam.

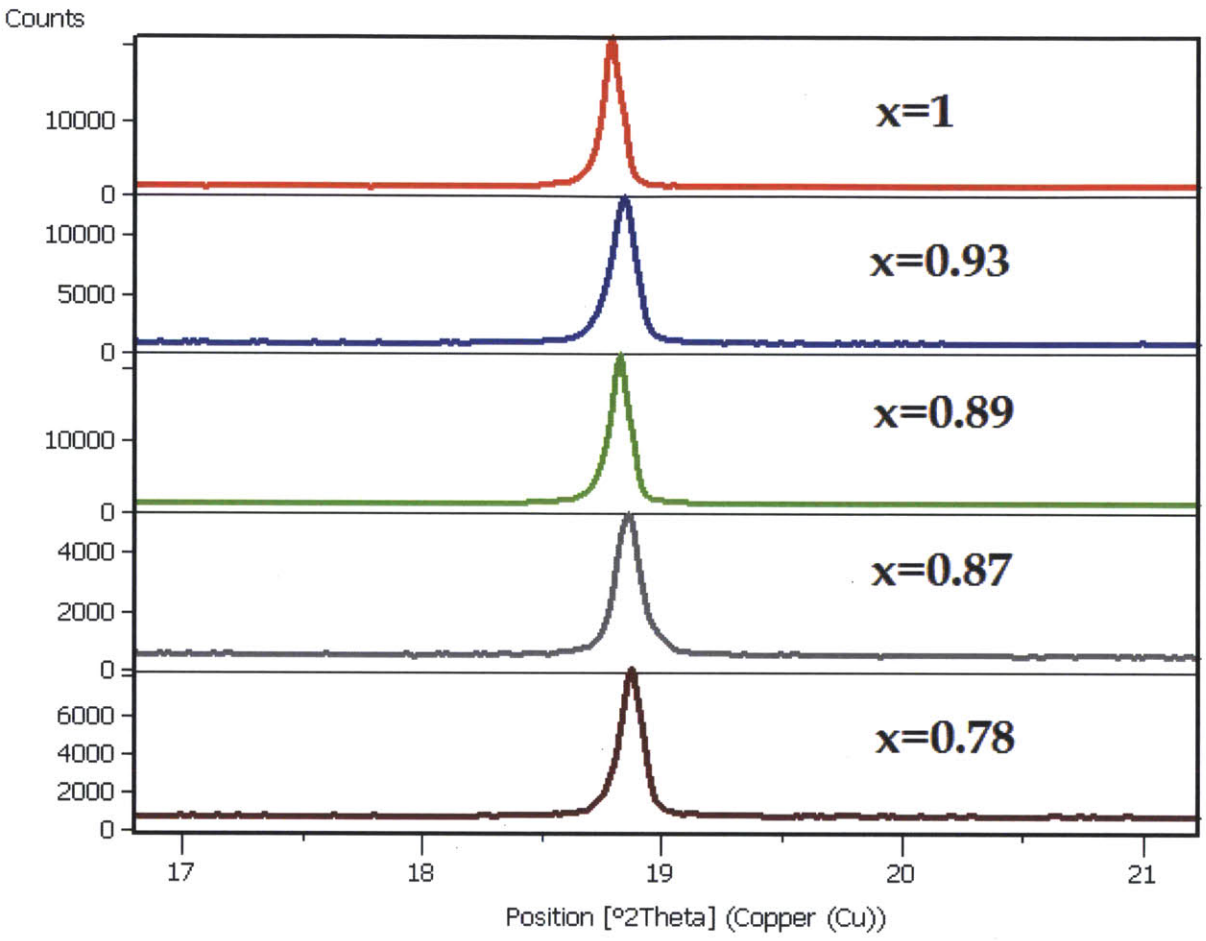

Figure 6.15: XRD profiles of disordered samples, focusing on one peak.

x in $Li_xNi_{0.5}Mn_{1.5}O_4$	Lattice Constant	R^2	χ^2	% Side Reaction
x = 1	8.175 Å+/- 0.001Å	5.68%	2.77	-
x = 0.93	8.164 Å+/- 0.001Å	3.99%	2.38	82.44%
x = 0.89	8.159 Å+/- 0.001Å	6.09%	2.37	44.84%
x = 0.87	8.157 Å+/- 0.001Å	1.17%	2.48	73.11%
x = 0.78	8.142 Å+/- 0.001Å	8.36%	2.34	63.36%

Table 6.3: Refinement data for disordered spinel XRD scans. These data refined much better than the ordered spinel, and R2 and χ^2 values were determined. Using the lattice constant, the approximate lithiation state was found (see figure 6.16, and discussion below). It should be noted that the amount of side reaction in these samples was apparently much greater than the amount of side reaction in the ordered samples. This lead to decreased sample breakage resulting in better XRD data, but also to a lower range of charge states sampled.

Unlike the ordered spinel samples, the disordered LNMO experienced no phase separation. It was thus necessary to use other means to determine the amounts of delithiation listed in table 6.3. To do this, these data representing known lattice constants and unknown charge state were compared to a dataset in which both charge state and lattice constant were known from reference 54. It was assumed that the sample as prepared was fully lithiated, which specified the point x=1 on the line defining a(x) in which a is the measured lattice constant and x is lithiation state in $LiNi_{0.5}Mn_{1.5}O_4$. The slope of this line was determined by the assumption:

$$\left[\frac{da}{dx}\right]_{Observed} = \left[\frac{da}{dx}\right]_{Literature}$$

Sample lattice constants were matched to the line defined by these two constraints (figure 6.16). This way, a slight difference in processing conditions – displacing the lattice constants of our sample at a given charge state, relative to those given in the literature – could be accounted for.

While a full range of lithiation states from 1 to 0 were targeted electrochemically, these disordered samples in particular exhibited a large discrepancy between the total amount of current run through the cell and the amount that actually contributed to sample delithiation (see the '% Side Reaction' column in Table 5.3). For a discussion of the tradeoffs involved in electrochemical titration of high-voltage cathodes, see section V(iv).

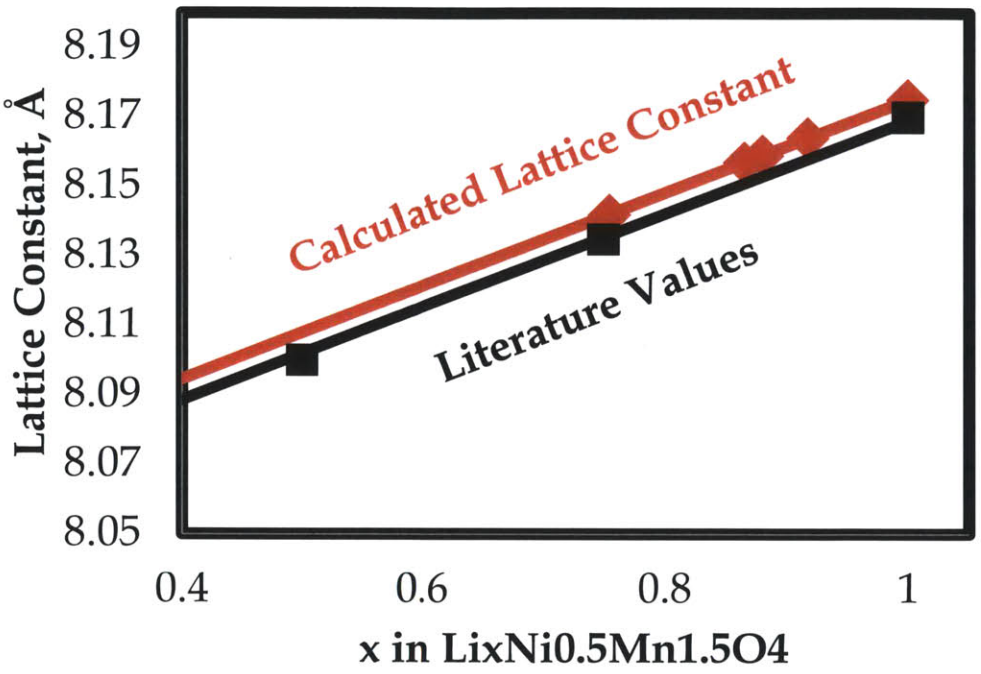

Figure 6.16: Comparison of sample lattice constant calculated from Rietveld refinement, to values in *Reference 54*.

Figure 6.17 shows the Arrhenius behavior of conductivity measured for the disordered samples, along with best fit lines calculated from these data. Activation energies were calculated from the slopes of these lines, as they were in the previous section VI (iv) for the ordered samples.

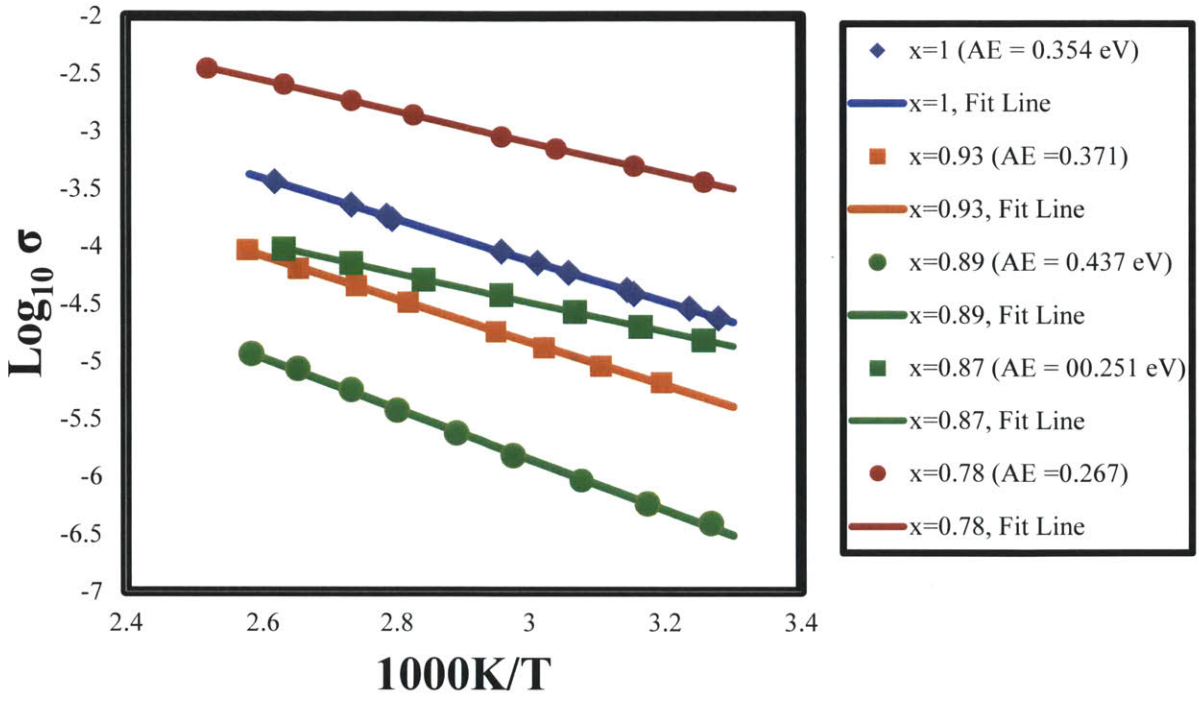

Figure 6.17: Conductivities of disordered samples measured via Van Der Pauw. These data can be interpreted in light of small polaron conduction, as giving higher conductivity at lithiation values corresponding to a mix of oxidation states.

Figure 6.18 graphs both the conductivity at 30°C (calculated from the best fit line) and the negative of the activation energy as a function of lithiation state (for the rationale behind this graph, see the previous section on the ordered spinel and figure 6.12). It is seen that general trends in conductivity track those in activation energy, involving a sharp minimum at x=0.87. A major exception to this is the datapoint at x=0.89, inn which the low activation energy would suggest a higher conductivity than actually measured. Electrochemical measurements show that 12% of the lithiation range occurs due to the $Mn^{3+} \leftrightarrow Mn^{4+}$ redox couple at 4V. Thus the conductivity and activation energy minima occur at the datapoint closest to the end of this 4V plateau, where the spinel is expected to be homogeneous in the oxidation states of both Mn and Ni. Further analysis of the correlations between oxidation state and electronic properties will occur in the following section.

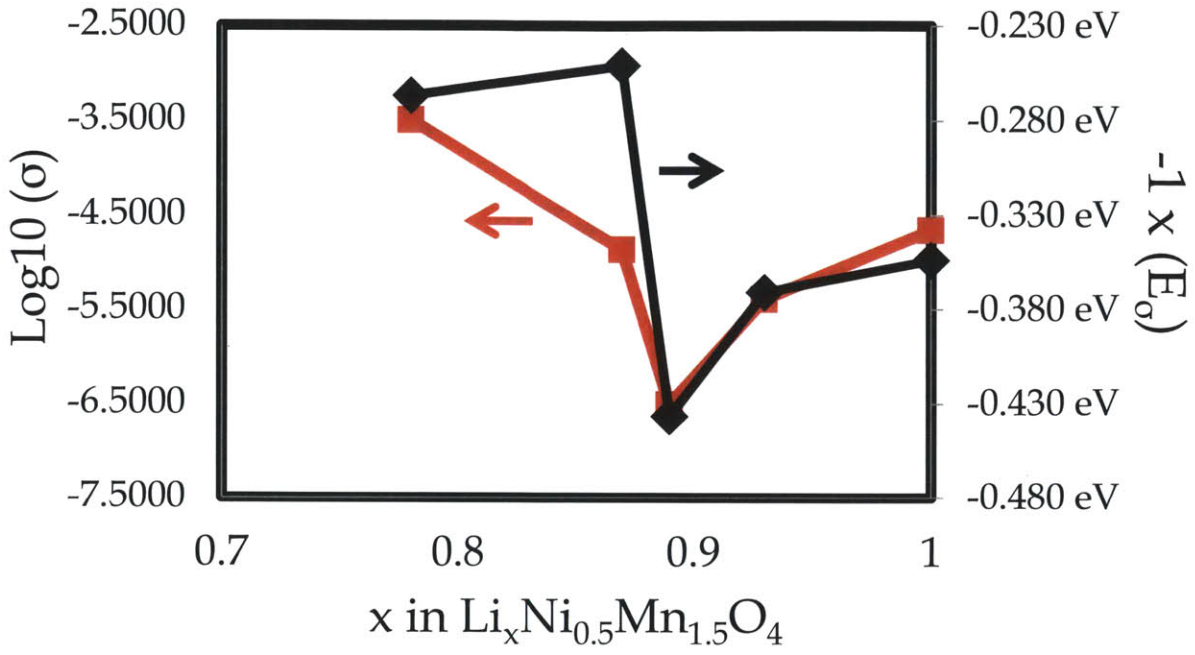

Figure 6.18: The evolution of conductivity and activation energy of the ordered spinel with charge state. While the conductivity appears to track the general trends of the activation energy, some changes in conductivity cannot be explained by changes in AE. This will be discussed in the following section.

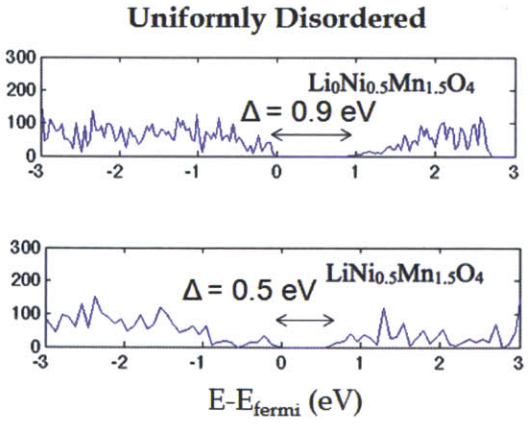

Figure 6.19: Bandstructure calculations on lithiated and delithiated, disordered LNMO. These calculations show a bandgap that is somewhat wider than the E_σ measured in the current work. However, the margin is low enough for the fully lithiated case that a definite conclusion cannot be drawn as to the nature of the measured activation energy. This is unlike the case of the ordered spinel, discussed above. (From *Ref 19*)

Figure 6.19 presents the bandstructure of the disordered spinel in both lithiated and fully delithiated states, calculated by our collaborators in the BATT project. Comparing the calculated bandgap of the fully lithiated disordered spinel to the measured activation energy E_σ it appears that, while $E_\sigma < E_g$, the difference is significantly smaller than that in the ordered spinel. Thus, further measurements would be required to determine whether E_σ represents mobility only or a combination of mobility and carrier generation.

f. Comparison of ordered vs. disordered conductivities and activation energies as a function of lithiation

The data presented allow one to compare the conductivities of the ordered and disordered spinel and make some inferences as to the origin of conductivity differences and changes. To this end, figure 6.20 presents the measured conductivities of the two spinels on the same graph.

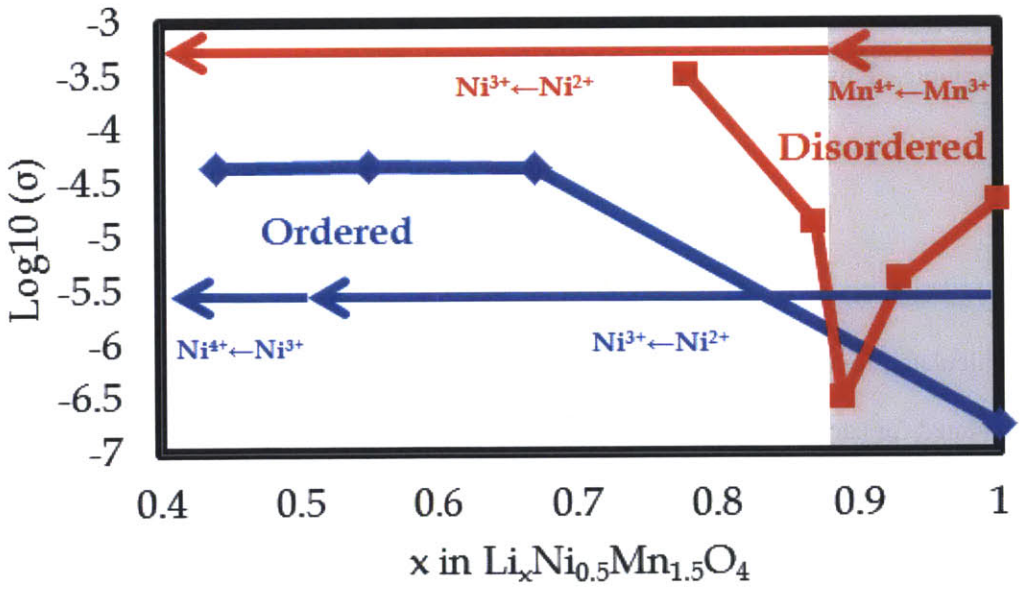

Figure 6.20: This plot shows the evolution of conductivity of both ordered and disordered polymorphs of LNMO with charge state. The regions corresponding to equilibrium redox couples are labeled. Greyed out region corresponds to the Mn plateau in disordered spinel. Arrows point in the direction of delithiation (ie. charge)

It is seen here that the conductivity of the disordered spinel begins (in the fully lithiated state) two orders of magnitude above that of the ordered spinel as discussed previously, and in agreement with the literature. Upon delithiaiton the conductivity of the disordered polymorph drops to approximately the level of the ordered polymorph. With further delithiation, the conductivity of the disordered material rises again. The conductivity of the ordered spinel rises monotonically with delithiation.

In almost all cases, the line fit to the Arrhenius temperature plot had an R^2 value between 0.999 and 1. The data were thus very linear, which suggests that the data can be treated as having Arrhenius behavior with prefactor σ_0 nearly temperature-independent. However, looking at the data in figure 6.20 suggests that σ_0 does have a dependence on oxidation state. This is because, while activation energy does often fall when conductivity rises, its motion does not appear to fully explain the change in conductivity. Thus, σ_0 must be a function of the mixture of oxidation states observed in the sample in accordance with the small polaron model of conduction.

More can be said about the origin of changes in conductivity by calculating the conductivity prefactor for each sample. This can be derived from the Arrhenius equation:

$$\sigma_{SP} = \sigma_0 e^{\frac{-E_\mu}{kT}}$$

$$ln(\sigma_{SP}) = ln(\sigma_0) - ln\left(E_\mu/_{kT}\right)$$

In which E_μ was calculated for each case above. σ_0, the intercept of the line fit to the conductivity data, has thus been calculated for each curve. These values are given in figure 6.21 and 6.22.

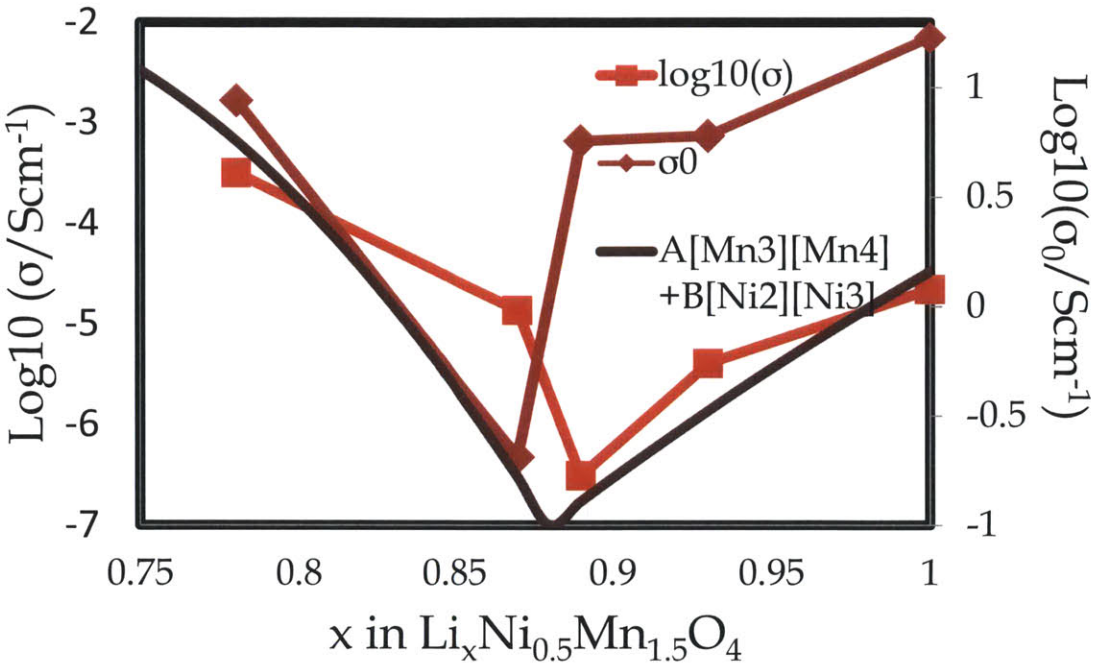

Figure 6.21: Conductivity, calculated σ_0, and sum of the products of equilibrium carrier concentrations in the disordered spinel and their evolution with delithiation. The sum of the products of carrier concentrations, in arbitrary units, has been shifted such that its zero corresponds to the lower limit of the vertical axis. This graph shows that conductivity appears to be influenced by but not dominated by carrier concentration.

In figure 6.21, we see that the conductivity of the disordered spinel tends to be low when $\log10(\sigma_0)$ is low and high when it is high. The minimum corresponds with the end of the 4V plateau in this material, at about x=0.88. This is expected, as from section III (iv) we see that in the polaron hopping conduction model:

$$\sigma_0 = c\,(1-c)\frac{q^2 a^2 \nu}{kT}$$

Thus the conductivity prefactor is expected to be proportional to the product of ion concentrations. In figure 6.21 we see the product $[Mn^{3+}][Mn^{4+}]$ (for x>0.88) and the product $[Ni^{2+}][Ni^{3+}]$ (for x<0.88) plotted in arbitrary units. This was calculated assuming an equilibrium carrier concentration along both voltage plateaus. At x=.12 we see that there is an expected deficit of carriers, explaining the minima in conductivity and σ_0. That these minima do not fully match, and that the measured σ_0 remains relatively

high at x=0.89, remain unexplained. They may have to do with energetic effects to do with the polaron strain field or the distortions required for ion hopping, as these quantities are clearly in flux as shown by the measurements of E_μ above. The relatively weak temperature dependence of σ_0 over the range measured was not considered.

In the case of the ordered spinel, it is seen that σ_0 is generally low where σ is low and high where σ is high. At intermediate values of lithiation there is apparently some change in σ_0 which is offset by changes in σ. Both of these values are at their lowest near x=1 where the sum of products $[Ni^{2+}][Ni^{3+}]+[Ni^{3+}][Ni^{4+}]$, representing the c(1-c) term in the formula for σ_0, is at its lowest. While the average value of σ_0 is higher at higher lithiation states, it has some variation which is offset by variation in E_σ (compare to figure 6.12). Were it possible to measure a fully delithiated sample, it is expected that its conductivity would be low due to the re-emergence of a homogeneous Ni oxidation state.

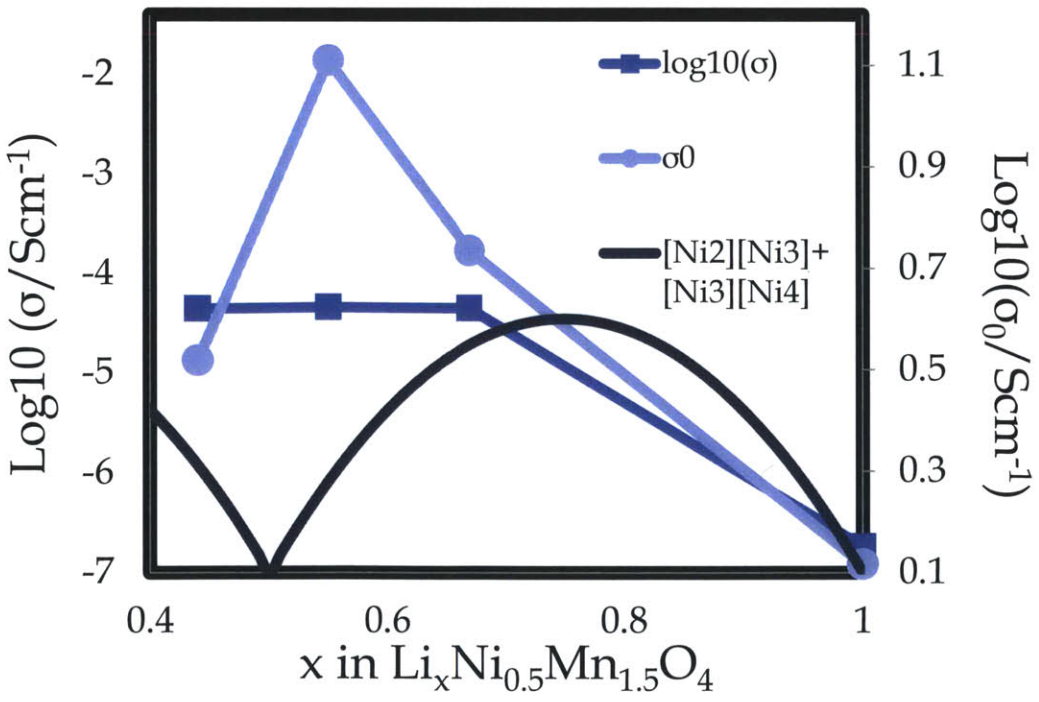

Figure 6.22: Conductivity, calculated σ_0, and product of equilibrium carrier concentrations in the ordered spinel and their evolution with delithiation. This graph shows that the sum of the products of carrier

concentrations is low at high values of x but not at intermediate values. This may be explained by a disproportionation reaction in the Ni^{3+} region.

It is important to note that there is not a significant drop in conductivity or in σ_0 near x=0.5, even though the equilibrium carrier concentration is low in this region. That is presumably because of the disproportionation reaction:

$$2Ni^{3+} \rightarrow Ni^{2+} + Ni^{4+}$$

By this reaction, carriers can be generated. Since the difference between the $Ni^{2+} \leftrightarrow Ni^{3+}$ and $Ni^{3+} \leftrightarrow Ni^{4+}$ voltage plateaus is small (about 0.05V as shown in reference 55) compared to the activation energy observed in the Arrhenius measurements presented above, this disproportionation reaction is free to generate carriers in the region of intermediate x. Thus, mobility rather than carrier density limits the conductivity in this region. Such a disproportionation cannot, however, generate carriers at high or low values of x. Therefore it is expected that both σ and σ_0 would have low values at x=0 as well.

While this material is seen to have reasonably high conductivity, it is significantly lower than the values required for the fabrication of electrodes without conductive additive (image II(iii), above).

VII. CONCLUSION

In this work, the electrical conductivity of the high-voltage spinel $Li_xNi_{1/2}Mn_{3/2}O_4$ was measured as a function of lithiation state. To the knowledge of the author, the only previously published datasets measuring LNMO conductivity were for the fully lithiated spinel. It is hoped that the data presented in the present work will aid in the design of positive electrodes for future high energy density lithium ion batteries.

It was shown that LNMO in the as-sintered state had a similar conductivity to samples measured in the literature, and have a similar dependence as a function of sintering temperature. Temperature-dependent measurements then elucidated the mechanisms by charge state (degree of lithiation) influenced the conductivity of the material. Concentrations of charge carriers appeared to influence but not dominate conductivity. Instead, thermal activation energy appeared to play a more dominant role. This thermal activation energy was compared to the bandgap calculated from DFT by our collaborators, and to polaron hopping energies of metal oxides studied in the literature. In this, it seemed that the measured thermal activation energy corresponded to carrier mobility rather than to carrier generation (though it is possible for the disordered spinel that thermal carrier generation was relevant for some lithiation states).

While a wide range of lithiation states were targeted *via* electrochemical titration of the LNMO samples, the range actually achieved was considerably narrower. This highlights a need for more stable electrolytes for high-voltage batteries.

APPENDIX A: VOLTAGE DROPS IN BATTERIES

This series of calculations is meant to provide an order of magnitude estimate of polarization losses in a cathode made of LNMO, in order to identify bottlenecks worthy of further investigative research. It is also meant to compare composite cathodes to additive-free sintered cathodes, in order to guide thoughts about the expected differences between the two.

In these calculations the effects accounted for are ionic conduction through the pores, electronic conduction through solid cathode, and ionic diffusion through solid cathode. Charge transfer at the cathode/electrolyte interface is neglected.

As each point in the cathode material corresponds to a current path of a different resistance, the cathode morphology will determine the distribution of currents and this distribution will, in turn, determine the effective electrode resistance. Unlike in Appendix D, an effort is not made to account for this. Quantities used are simple averages over the entire electrode.

Conductivities, specific surface area, and ionic concentrations are order of magnitude estimates based on reasonable assumptions. Ohm's law was used to calculate voltage drops. The Nernst-Einstein equation was used to calculate Li mobility from an average diffusivity value.

APPENDIX A TABLE 1: ADDITIVE-FREE SINTERED CATHODE

Ionic Current in Pores		**Electronic Current through Solid**		**Ionic Current through Solid**	
Electrolyte Ionic Conductivity:	7.8×10^{-3} S/cm	LNMO Electronic Conductivity:	5×10^{-5} S/cm	[Li+]:	Half theoretical capacity of 147mAh/g
C-Rate:	C/10	V Fraction Solid:	70 %	Chem. Diffusivity, LNMO:	4×10^{-12} cm^2/s
V Fraction Electrolyte:	32 %			Sp Surf. Area:	3.5×10^{7} cm^2/g
Thickness:	400 μm				
Voltage:	**0.022V**	**Voltage:**	**1.047 V**	**Voltage:**	**9×10^{-7}V**

Thus, in additive free sintered cathodes about 98% of the voltage drop is estimated to come from the electronic current flowing through the solid electrode. About 2% of the voltage drop appears to be the result of ionic resistance through the electrolyte.

APPENDIX A, TABLE 2: COMPOSITE CATHODE

Ionic Current in Pores		**Electronic Current through Conductive Carbon**		**Ionic Current through LNMO**		**Electronic Current Through LNMO**	
Electrolyte Ionic Conductivity:	7.8×10^{-3} S/cm	Graphite Electronic Conductivity:	5.8×10^{-4} S/cm	Sp Surf. Area:	3.5×10^{7} cm^2/g	LNMO El. Conductivity:	5×10^{-5} S/cm
C-Rate:	C/10	V Fraction Graphite:	10 %	Chem Diffusivity of LNMO:	$4\times10^{-12}cm^2/s$		
Thickness:	60 μm			[Li+]:	Half theoretical capacity of 147mAh/g		
V Fraction Electrolyte:	20 %						
Voltage:	**7×10^{-4} V**	**Voltage:**	**4.1×10^{-8} V**	**Voltage:**	**9×10^{-7} V**	**Voltage:**	**3×10^{-9} V**

According to this simple model, 100% of the voltage drop is due to ionic current passing through the pores with 0.1% due to ionic current in the active material. This has several implications. Firstly, *reference 9* reported a dependence of rate performance on amount of conductive carbon added. Since the calculated voltage drop due to electronic current through the carbon is so low, this dependence must indicate that for low amounts of carbon loading a percolating conductive network was not formed.

Secondly, as the voltage drop due to ionic conductivity through the active material is so low it is likely that Li does not take the shortest possible path through the active material. Instead, its path is distributed through both LNMO and electrolyte so as to avoid tortuosity in the pores. This would cause ionic diffusivity to have some influence on rate capability; otherwise it is not clear from this calculation how it is possible that the disordered and ordered spinel could have differences in rate capability.

APPENDIX B: EXPERIMENTAL PROCEDURES

Sintering pellets

1. Lithium Nickel Manganese Oxide powder was supplied from NEI corporation. To make a pellet, 300 mg of powder was measured and loaded into a stainless steel die measuring ½" diameter. 15,000 lbs of pressure was applied using a hydraulic press. Pressure was applied for 1 minute, at the end of which it had dropped due to normal hydraulic creep. Pressure was topped off to 15,000 lbs and held for another minute. Pressure was then released and the pellet taken from the die. No binder was used.
2. Pellets were loaded onto an alumina crucible cover and covered by an alumina crucible. No packing powder was used. Assembly was heated in a box furnace. Ramp up times were 1.5h to three hours; sinter temperatures and times were varied between sample batches.
3. Volume fractions of solid sample, open and closed porosities were measured via a four-point Archimedes measurement. Isopropanol was used as the suspension fluid.

Making Additive-Free Sintered Cathodes

1. Sintered pellets were attached to polishing die using Thermoweb 'Super Tape' Double-Sided Sheets. Both sides were polished with lapping paper, using 9um Si Carbide and 3um Alumina paper from South Bay Technologies. No lubricant was used (ie. samples were polished dry). Isopropanol was employed to remove samples from the adhesive. Thickness of the pellets was measured using calipers with an accuracy of ~2um.
2. The polished pellets were cut using a diamond-coated steel wire saw.
3. Cathodes masses were measured using a 7-point scale.
4. A mechanical pencil (#2 lead, 0.7mm, Bic) was employed to carbon coat one side of each sample to lower contact resistance with current collector.
5. Cathodes were dried at 120°C in vacuum for 48 hours to remove all moisture.

Making Conventional Cathodes

Procedure based on Reference 55, and discussed with X. Ma.

1. LNMO powder, from sintered pellets crushed in a mortar, was dried overnight at 120C in vacuum. All subsequent steps performed in Ar-filled glovebox.
2. Mixed 160 mg of LNMO and 30 mg of Super P carbon black in a mortar. Proceeded to mix, using a pestle, for 30 minutes. Super P was stored in glovebox.
3. Added 10 mg of PTFE 8A, large grain Teflon powder, from DuPont. This was purchased from a third party plastics parts supplier, as DuPont does not sell small quantities of this powder. PTFE was stored in glovebox.
4. Rolled mixture on a stainless steel plate. Folded, then repeated 6-8 times to mix completely
5. Used a 5/16" punch to make cathode disks. Rolled the punched disk, then punched again. Repeated several times to get thin samples. Aimed for ~3mg/cm2, roughly 30-40μm thick.

Assembling Swagelok Cells

1. Washed Swagelok cells and dried at 120°C for 48h in vacuum. All subsequent steps were performed in an Ar glovebox.
2. Metallic lithium foil was punched with a ½" punch to be used as the anode. This was placed into an open Swagelok casing. 2 pieces of ½" diameter Celgard C480 separator were placed on top.
3. The cathode was added along with 70ul of electrolyte (1M LiPF6 in 1:1 Ethylene Carbonate : Diethyl Carbonate , EC:DEC by volume; all components from Sigma Aldrich). The cell was sealed.

Electrochemical Tests

- Electrochemical delithiation was done galvalostatically at C/300. After cathode had been delithiated the required amount, it was allowed to stand for 1 day to allow Li gradients to equilibrate.

- Cell cycling was performed galvanostatically at C/5. Cell was charged to 5V and held for 1hour. Cell was discharged galvanostatically at C/5 to 3V, and held for 1hour.

Van Der Pauw Tests

1. Samples were carefully removed from Swagelok cells in an Ar glovebox. They were placed in a vial and washed 3 times with Diethyl Carbonate (DEC). They were then allowed to stand overnight in DEC. All subsequent steps occurred in a glovebox.
2. Samples were washed with Isopropanol (IPA) 3 times. They were then dried briefly at room temperature. Both sides were polished with 3um lapping paper in order to remove the conductive carbon coating as well as any surface salts.
3. Sample thickness was measured using calipers.
4. Conductive carbon paste was applied to samples in order to form 4 contacts. Samples were dried for 1hour at 110C on a hotplate.
5. Samples were moved to Van Der Pauw test setup. Four probes were carefully applied to sample contacts.
6. Current was run through probes and voltage measured in order to check contacts. Two contacts were tested at once (ie. AB, then BC, CD, DA).
7. Van Der Pauw measurements were performed by holding voltage between two contacts constant at 0.2V and measuring the current through the other two contacts. Recorded steady state current, after any transient had died out.
8. Adjusted voltage of thermoelectrics in sample stage and waited for temperature to stabilize. Repeated VDP measurement at new temperature.
9. Conductivity was calculated from data collected using Mathematica. Fit line was calculated and data were plotted using Excel.
10. Sample was removed from glovebox and XRD scan was run.

APPENDIX C: SAMPLE INDEX

Ordered, Sample A *Delithiation*			
Calculated x in $Li_xNi_{1/2}Mn_{3/2}O_4$:	x=1	**Mass beginning Delithiation:**	(not delithiated)
Phase I:	8.169Å (100 wt%)	**Theoretical Capacity:**	-
Phase II:	-	**Electrochemical Target x:**	-
Phase III:	-	**Delithiation Efficiency:**	-
Porosity:	73%		
Van Der Pauw			
Thickness upon VDP Measurement:	425 µm	**E_σ:**	0.412 eV
Log_{10}(Conductivity) at 30C:	-6.74	**$Log_{10}(\sigma_0)$:**	0.116
		R^2 of fit line:	0.9945

Ordered, Sample F *Delithiation*			
Calculated x in $Li_xNi_{1/2}Mn_{3/2}O_4$:	x=0.67	**Mass beginning Delithiation:**	0.083271 g
Phase I:	8.156Å (33 wt%)	**Theoretical Capacity:**	0.01224084 Ah
Phase II:	8.083 Å (67 wt%)	**Electrochemical Target x:**	x=0.4
Phase III:	-	**Fraction Side Reaction:**	45%
Porosity:	73%		
Van Der Pauw			
Thickness upon VDP Measurement:	250 µm	**E_σ:**	0.306 eV
Log_{10}(Conductivity) at 30C:	-4.35	**$Log_{10}(\sigma_0)$:**	0.735
		R^2 of fit line:	0.9995

Ordered, Sample C *Delithiation*			
Calculated x in $Li_xNi_{1/2}Mn_{3/2}O_4$:	x=0.55	**Mass beginning Delithiation:**	0.082067 g
Phase I:	8.169Å (10 wt%)	**Theoretical Capacity:**	0.01206385 Ah
Phase II:	8.096Å (10 wt%)	**Electrochemical Target x:**	x=0.55
Phase III:	-	**Fraction Side Reaction:**	0.3 % (within error)
Porosity:	75%		
Van Der Pauw			
Thickness upon VDP Measurement:	380 μm	**E_σ:**	0.327 eV
Log_{10}(Conductivity) at 30C:	-4.33	**$Log_{10}(\sigma_0)$:**	1.11
		R^2 of fit line:	0.9992

Ordered, Sample D *Delithiation*			
Calculated x in $Li_xNi_{1/2}Mn_{3/2}O_4$:	x=0.44	**Mass beginning Delithiation:**	0.086649 g
Phase I:	-	**Theoretical Capacity:**	0.01273740 Ah
Phase II:	8.088Å (87 wt%)	**Electrochemical Target x:**	x=0.2
Phase III:	8.005Å (13 wt%)	**Fraction Side Reaction:**	44%
Porosity:	71%		
Van Der Pauw			
Thickness upon VDP Measurement:	375 μm	**E_σ:**	0.293 eV
Log_{10}(Conductivity) at 30C:	-4.36	**$Log_{10}(\sigma_0)$:**	0.517
		R^2 of fit line:	0.9969

Disordered, Sample D *Delithiation*			
Calculated x in $Li_xNi_{1/2}Mn_{3/2}O_4$:	x=1	**Mass beginning Delithiation:**	(not delithiated)
Lattice Constant:	8.175 Å (Single Phase)	**Theoretical Capacity:**	-
Electrochemical Target x:	-	**Fraction Side Reaction:**	-
Porosity:	66%		
Van Der Pauw			
Thickness upon VDP Measurement:	460 μm	**E_σ:**	0.354 eV
Log_{10}(Conductivity) at 30C:	-4.66	**$Log_{10}(\sigma_0)$:**	1.23
		R^2 of fit line:	0.9998

Disordered, Sample E *Delithiation*			
Calculated x in $Li_xNi_{1/2}Mn_{3/2}O_4$:	x=0.93	**Mass beginning Delithiation:**	0.139279 g
Lattice Constant:	8.164 Å (Single Phase)	**Theoretical Capacity:**	0.02047401 Ah
Electrochemical Target x:	x=0.6	**Fraction Side Reaction:**	82%
Porosity:	73%		
Van Der Pauw			
Thickness upon VDP Measurement:	500 μm	**E_σ:**	0.371 eV
Log_{10}(Conductivity) at 30C:	-5.39	**$Log_{10}(\sigma_0)$:**	0.780
		R^2 of fit line:	0.9994

Disordered, Sample F *Delithiation*			
Calculated x in $Li_xNi_{1/2}Mn_{3/2}O_4$:	x=0.89	**Mass beginning Delithiation:**	0.097904 g
Lattice Constant:	8.159 Å (Single Phase)	**Theoretical Capacity:**	0.01439189 Ah
Electrochemical Target x:	x=0.8	**Fraction Side Reaction:**	45%
Porosity:	77%		
Van Der Pauw			
Thickness upon VDP Measurement:	485 μm	**E_σ:**	0.437 eV
Log_{10}(Conductivity) at 30C:	-6.51	**$Log_{10}(\sigma_0)$:**	0.756
		R^2 of fit line:	0.9987

Disordered, Sample I *Delithiation*			
Calculated x in $Li_xNi_{1/2}Mn_{3/2}O_4$:	x=0.87	**Mass beginning Delithiation:**	0.107236 g
Lattice Constant:	8.157 Å (Single Phase)	**Theoretical Capacity:**	0.01576369 Ah
Electrochemical Target x:	x=0.52	**Fraction Side Reaction:**	73%
Porosity:	73%		
Van Der Pauw			
Thickness upon VDP Measurement:	434 μm	**E_σ:**	0.251 eV
Log_{10}(Conductivity) at 30C:	-4.86	**$Log_{10}(\sigma_0)$:**	-0.689
		R^2 of fit line:	0.9996

Disordered, Sample C *Delithiation*			
Calculated x in $Li_xNi_{1/2}Mn_{3/2}O_4$:	x=0.78	**Mass beginning Delithiation:**	0.087811 g
Lattice Constant:	8.142 Å (Single Phase)	**Theoretical Capacity:**	0.01290822 Ah
Electrochemical Target x:	x=0.4	**Fraction Side Reaction:**	63%
Porosity:	77%		
Van Der Pauw			
Thickness upon VDP Measurement:	509 μm	**E_σ:**	0.267 eV
Log_{10}(Conductivity) at 30C:	-3.500	**$Log_{10}(\sigma_0)$:**	0.942
		R^2 of fit line:	0.9998

APPENDIX D: CELL AND PACK LEVEL DILUTIONS

Masses of components from analysis in *reference 73*.Volumes calculated based on estimated densities.

COMPONENT	MASS (G)	MASS %	APPROX. VOLUME (CC)	VOL %
Anode Material	564 g	16%	256 cc	30%
Binder	70 g	2%	39 cc	5%
Current Collector	152 g	4%	17 cc	2%
Cathode Material	1409 g	41%	276 cc	33%
Conductive Carbon	46 g	1%	21 cc	3%
Binder	93 g	3%	52 cc	6%
Current Collector	63 g	2%	23 cc	3%
Tabs, End Plates	66 g	2%	8 cc	1%
Core	1 g	-	Negligible	-
Container	291 g	8%	108 cc	13%
Electrolyte	618 g	18%	Negligible V. Added	-
Separator	61 g	2%	40 cc	5%
TOTAL:	3433 g		842 cc	
ACTIVE TOTAL:	1972 g	57%	532 cc	63%

= Active Intercalation Material

= Could be reduced by adopting electrode architecture with higher loading

= Other

REFERENCES

(1) Keyser, P. T. "The Purpose of the Parthian Galvanic Cells: A First-Century A. D. Electric Battery Used for Analgesia". *J. Near Eastern Stud.* 52, 2, 81-98 (1993)

(2) USABC Goals for Advanced Batteries for EVs http://www.uscar.org/guest/article_view.php?articles_id=85 (Accessed Nov. 28, 2012)

(3) Woodford, W. H. Ransil, A. Chiang, Y.-M. "Advanced Batteries: 'Beyond Li-Ion'". NPC Future Transportation Fuels Study: Advancing Technology for America's Transportation Future. Study Topic Papers, Paper #17 (2012)

(4) Scrosati, B. "Lithium Rocking-Chair Batteries: An Old Concept?" *J. Electrochem. Soc.* 193. 10. 2776-2781. (1992)

(5) Tarascon, J.-M. Armand, M. "Issues and challenges facing rechargeable lithium batteries" *Nature* 414, 359-367. (2001)

(6) Duduta, M. Ho, B. Wood, V. C. Limthongkul, P. Brunini, V. E. Carter, W. C. Chiang, Y. M. "Semi-Solid Lithium Rechargeable Flow Battery" *Adv. Energy Mat.* 1, 511–516 (2011)

(7) Lu, Y. Goodenough, J. B. "Rechargeable alkali-ion cathode-flow battery" *J. Mater. Chem.*, 21, 10113-10117 (2011)

(8) Hamelet, S. Tzedakis, T. Leriche, J.-B. Sailler, S. Larcher, D. Taberna, P.-L. Simon, P. Tarascon, J.-M. "Non-Aqueous Li-Based Redox Flow Batteries" *J. Electrochem. Soc.* 159, 8, A1360-A1367 (2012)

(9) Girishkumar, G.; McCloskey, B.; Luntz, A. C.; Swanson, S.; Wilcke, W. "Lithium-Air Battery: Promise and Challenges" J. Phys.Chem. Lett. 2010, 1, 2193–2203.

(10) Bruce, P. G.; Hardwick, L. J.; Abraham, K. M. "Lithium-air and lithium-sulfur batteries" MRS Bull. 2011, 36, 506–512.

(11) Christensen, J.; Albertus, P.; Sanchez-Carrera, R. S.; Lohmann, T.; Kozinsky, B.; Liedtke, R.; Ahmed, J.; Kojic, A. "A Critical Review of Li/Air Batteries" J Electrochem Soc 2012, 159, R1–R30.

(12) Liu, N. Wu, H. McDowell, M. T. Yao, Y. Wang, C. Cui, Y. "A Yolk-Shell Design for Stabilized and Scalable Li-Ion Battery Alloy Anodes" Nano Lett. 12 (6), pp 3315–3321 (2012)

(13) Magasinski, A. Dixon, P. Hertzberg, B. Kvit, A. Ayala, J. Yushin, G. "High-performance lithium-ion anodes using a hierarchical bottom-up approach." Nature Mater. 9, 353-358. (2010)

(14) Zhou, H. Upreti, S. Chernova, N. A. Hautier, G. Ceder, G. Whittingham, S. M. "Iron and Manganese Pyrophosphates as Cathodes for Lithium-Ion Batteries" Chem. Mater. 23, 293–300 (2011)

(15) Barpanda , P. Nishimura, S-I. Yamada, A. "High-Voltage Pyrophosphate Cathodes" Adv. Energy Mater. 2, 841–859 (2012)

(16) Mueller, T. Hautier, G. Jain, A. Ceder, G. "Evaluation of Tavorite-Structured Cathode Materials for Lithium-Ion Batteries Using High-Throughput Computing" Chem. Mater. 110817062108016 (2011)

(17) Ceder, G. Van der Ven, A. "Phase diagrams of lithium transition metal Oxides : investigations from first principles" Electrochimica Acta 45 131-150. (1999)

(18) Delmas, C. Maccario, M. Croguennec, L. Le Cras, F. Weill, F. "Lithium deintercalation in LiFePO4 nanoparticles via a domino-cascade model" Nature Mat. 7, 665-671. (2008)

(19) Persson, K. Lee, E. "The Li(Ni0.5Mn1.5)O2 spinel from first principles" Batteries for Advanced Transportation Technologies, Spinel Focus Group Update (January 2012)

(20) Kang, B. Ceder, G. "Battery materials for ultrafast charging and discharging" Nature 458, 190-193 (2009)

(21) Scharner S, Weppner W, Schmid-Beurmann P. "Evidence of Two-Phase Formation upon Lithium Insertion into the Li1.33Ti1.67O4 Spinel" J. Electrochem. Soc. 146 (3), 857-861. (1999)

(22) Panero S, Reale P, Ronci F, Scrosati B, Perfetti P. "Refined, in-situ EDXD Structural Analysis of the Li[Li1/3Ti5/3]O4 Electrode Under Lithium Insertion-Extraction." Phys. Chem. Chem. Phys. 3, 845-847. (2001)

(23) Wagemaker, M. Simon, D. Kelder, E. Schoonman, J. Ringpfeil, C. Haake, U. Lutzenkirchen-Hecht, D. Frahm, R. Mulder, F. "A Kinetic Two-Phase and Equilibrium Solid Solution in Spinel Li4+xTi5O12" *Adv. Mat.* 18. 3169-3173. (2006)

(24) Ariyoshi, K. Yamamoto, S. Ohzuku, T. "Three-volt lithium-ion battery with Li[Ni1/2Mn3/2]O4 and the zero-strain insertion material of Li[Li1/3Ti5/3]O4" J. Pwr. Srcs. 119–121 959–963. (2003)

(25) Jung, H-G. Jang, M. W. Hassoun, J. Sun, Y.-K. Scrosati, B. "A high-rate long-life Li4Ti5O12/Li[Ni0.45Co0.1Mn1.45]O4 lithium-ion battery" Nature Communications, 2:516 (2011)

(26) Verwey, E. J. Haayman, P. W. Romejyn, F. C. "Physical Properties and Cation Arrangement of Oxides with Spinel Structures" J. Chem. Phys. 15, 181 (1947)

(27) Ilhe, D. Lorentz, B. "Small-polaron conduction and short-range order in Fe3O4" J. Phys. C: Solid State Phys. 19 5239-5251. (1986)

(28) Degiorgi, L. Wachter, P. Ilhe, D. "Small-polaron conductivity in magnetite" Phys. Rev. B. 35; 17. 9259-9264. (1987)

(29) Dorris, S. E. Mason, T. O. "Electrical Properties and Cation Valencies in Mn3O4" J. Am. Ceram. Soc. 71; 5. 379-385 (1988)

(30) Pistoia, G. Zane, D. Zhang, Y. "Some Aspects of LiMn2O4 Electrochemistry in the 4Volt Range" *J. Electrochem. Soc.* 142, 8. 2551-2557. (1995)

(31) Molenda, J. Marzec, J. Swierczek, K. Palubiak, D. Ojczyk, W. Ziemnicki, M. "The effect of 3d substitutions in the manganese sublattice on the electrical and electrochemical properties of manganese spinel" *Solid State Ionics*. 175. 297-304. (2004)

(32) Molenda, J. Swierczek, K. Kucza, W. Marzec, J. Stoklosa, A. "Electrical properties of LiMn2O4-d at temperatures 220-1100K" *Solid State Ionics*. 123. 155-163. (1999)

(33) Austin, I. G. Mott, N. F. "Polarons in crystalline and non-crystalline materials" Advances in Physics, 18:71, 41-102 (1969)

(34) Holstein, T. "Studies of Polaron Motion Part II: The 'Small' Polaron" Ann. Phys. 8, 343-389 (1959)

(35) Chiang, Y.-M. Lavik, E. B. Blo, D. A. "Defect Thermodynamics and Electrical Properties of Nanocrystalline Oxides: Pure and Doped CeO2" Nanostruct. Mats, 9. 633-642 (1997)

(36) Tuller, H. L. Nowick, A. S. "Small Polaron Electron Transport In Reduced CeO2 Single Crystals" J. Phys. Chem. Solids. 38, 859-867. (1977)

(37) Tuller, H. L. Nowick, A. S. "Defect Structure and Electrical Properties of Nonstoichiometric CeO Single Crystals" J. Electrochem. Soc., Volume 126, Issue 2, Pages 209-217 (1979)

(38) Naik, I. K. Tien, T. Y. "Small-Polaron Mobility on Nonstoichiometric Cerium Dioxide" J. Phys. Chem. Solids, 39, 311-315 (1978)

(39) Dygas, J. R. Kopec, M. Krok, F. Lisovytskiy, D. Pielaszek, J. "Conductivity and dielectric relaxation phenomena in lithium manganese spinel" Solid State Ionics 176 2153 – 2161. (2005)

(40) Ponpandian, N. Balaya, P. Narayanasamy, A. "Electrical conductivity and dielectric behaviour of nanocrystalline NiFe2O4 spinel" J. Phys.: Condens. Matter 14 3221–3237. (2002)

(41) Nishizawa, M. Tomoaki, I. Hiromichi, K. Itoh, T. Uchida, I. "Electrochemical In-Situ Conductivity Measurements for Thin Film of Li1-xMn2O4 Spinel". *Chem. Mat.* 12, 1367-1371 (2000)

(42) Goodenough, J. B. Manthiram, A. Wnetrzewski, B. "Electrodes for Lithium Batteries". J. Pwr. Src. *4344 269-275.* (1993)

(43) Mohamedi, M. Makino, M. Dokko, K. Itoh, T. Uchida, I. "Electrochemical Investigation of LiNi0.5Mn1.5O4 thin film intercalation electrodes" *Electrochim. Acta* 48. 79-84. (2002)

(44) Zhong, Q. Bonakdarpour, A. Zhang, M. Gao, Y. Dahn, J. R. "Synthesis and Electrochemistry of LiNixMn2-xO4". *J. Electrochem. Soc.* 144, 1, 205-213. (1997)

(45) Gao, Y. Myrtle, K. Zhang, M. Reimers, J. N. Dahn, J. R. "Valence Band of LiNixMn2-xO4 and its effects on the Voltage Profiles of LiNixMn2-xO4/Li electrochemical cells." *Phys. Rev. B.* 54, 3, 16 670-16 675. (1996)

(46) Sun, Y.K. Jin, S.H. "Synthesis and electrochemical characteristics of spinel phase LiMn2O4-based cathode materials for lithium polymer batteries". *J. Mat. Chem.* 8, 11, 2399-2404. (1998)

(47) Pistoia, G. Antonini, A. Rosati, R. "Doped Li-Mn Spinels: Physical/Chemical Characteristics and Electrochemical Performance in Li Batteries". *Chem. Mat.* 9, 1443-1450. (1997)

(48) Ariyoshi, K. Iwakoshi, Y. Nakayama, N. Ohzuku, T. "Topotactic Two-Phase Reactions of Li[Ni1/2Mn3/2]O4 (P4332) in Nonaqueous Lithium Cells". *J. Electrochem. Soc.* 151 (2) A296-A303 (2004)

(49) Kim, J. Yoon, C. Myung, S. Prakash, J. Sun, Y. "Phase Transitions In Li1-dNi0.5Mn1.5O4 during Cycling at 5V" *J. Electrochem. Soc.* 7. 7. A216-A220. (2004)

(50) Lee, E. Persson, K. "Revealing the coupled cation interactions behind the electrochemical profile of LixNi0.5Mn1.5O4" *En. Env. Sci.* Accepted manuscript. (2012)

(51) Pasero, D. Reeves, N. Pralong, V. West, A. R. "Oxygen Nonstoichiometry and Phase Transitions in LiMn1.5Ni0.5O4-δ" *J. Electrochem. Soc.* 155 (4) A282-A291 (2008)

(52) Kunderaci, M. Amatucci, G. "Synthesis and Characterization of Nanostructured 4.7V LixMn1.5Ni0.5O4 Spinels for High-Power Lithium-Ion Batteries" *J. Electrochem. Soc.* 153 (7) A1345-A1352 (2006)

(53) Shaju, K. Bruce, P. "Nano-LiNi0.5Mn1.5O4 spinel: a high power electrode for Li-ion batteries" *Dalton Trans.* 5471-5475 (2008)

(54) Kim, J. Myung, S. Yoon, C. Kang, S. Sun, Y. "Comparative Study of LiNi0.5Mn1.5O4-δ and LiNi0.5Mn1.5O4 Cathodes Having Two Crystallographic Structures: Fd-3m and P4332" *Chem. Mater.* 16, 906-914. (2004)

(55) Ma, X. Kang, B. Ceder, G. "High Rate Micron-Sized Ordered LiNi0.5Mn1.5O4" *J. Electrochem. Soc.* 157 (8) A925-A931. (2010)

(56) Bard, A. J; Faulkner, L. R. "Electrochemical Methods. Fundamentals and Applications" 2nd Ed. Wiley, New York. ISBN 0-471-04372-9 (2001)

(57) Zhu, Y. Wang, C. "Galvanostatic Intermittent Titration Technique for Phase-Transformation Electrodes" *J. Phys. Chem. 114,* 2830–2841 (2010)

(58) Han, B. Van Der Ven, A. Morgan, D. Ceder, G. "Electrochemical modeling of intercalation processes with phase field models" *Electrochimica Acta.* 49. 4691-4699. (2004)

(59) Aurbach, D. Levi, M. Levi, E. Teller, H. Markovsky, M. Salitra, G. "Common Electroanalytical Behavior of Li Intercalation Processes into Graphite and Transition Metal Oxides" *J. Electrochem. Soc.* 145, 9. 3024-3034. (1998)

(60) Cogswell, D. A. Bazant, M. Z. "Coherency Strain and the Kinetics of Phase Separation in LiFePO4 Nanoparticles". ACS Nano 6, 3, 2215–2225. (2012)

(61) Bai, P. Cogswell, D. A. Bazant, M. Z. "Suppression of Phase Separation in LiFePO4 Nanoparticles During Battery Discharge" Nano Letters *11* (11), 4890–4896. (2011)

(62) Kim, J. Myun, S. Yoon, C. Oh, I. Sun, Y. "Effect of Ti Substitution for Mn on the Structure of LiNi0.5Mn1.5-xTixO4 and Their Electrochemical Properties as Lithium Insertion Material" *Journ. Electrochem. Soc.* 151 (11) A1911-A1918 (2004)

(63) Zhang, H. Yu, X. Braun, P. V. "Three-dimensional bicontinuous ultrafast-charge and -discharge bulk battery electrodes" Nat. Nanotech, 6, 277-281. (2011)

(64) Arunkumar, T. Manithram, A. "Influence of Lattice Parameter on Differences on the Electrochemical Performance of the 5V Spinel LiMn1.5-yNi0.5-zMy+zO4 (M=Li, Mg, Fe, Co, and Zn)" *Electrochem. S.S. Let.* 8 (8) A403-A405 (2005)

(65) Terada, Y. Yasaka, K. Nishikawa, F. Konishi, T. Yoshio, M. Nakai, I. "In Situ XAFS Analysis of Li(Mn, M)2O4 (M=Cr, Co, Ni) 5V Cathode Materials for Lithium-Ion Secondary Batteries". *Journal of Solid State Chemistry* 156, 286-291. (2001)

(66) Arunkumar, T. Manthiram, A. "Influence of Chromium Doping on the Electrochemical Performance of the 5 V spinel cathode LiMn1.5Ni0.5O4" *Electrochim. Acta* 50 5568-5572. (2005)

(67) Yang, M. Xu, B. Cheng, J. Pan, C. Hwang, B. Meng, Y. "Electronic, Structural, and Electrochemical Properties of LiNixCuyMn2-x-yO4 (0<x<0.5<y<0.5) High-Voltage Spinel Materials" *Chem. Mat.* 23. 2832-2841. (2011)

(68) Liu, J. Manthiram, A. "Understanding the Improved Electrochemical Performances of Fe-Substituted 5V Spinel Cathode LiMn1.5Ni0.5O4". *J. Phys. Chem. C* 112, 15073-15079. (2009)

(69) Wang, H. Xia, H. Lai, M. O. Lu, L. "Enhancements of rate capability and cyclic performance of spinel LiNi0.5Mn1.5O4 by trace Ru-doping" Electrochemistry Communications 11 1539–1542 (2009)

(70) Van Der Pauw, L. J. "A Method of Measuring Specific Resistivity and Hall Effect of Discs of Arbitrary Shape". Philips Research Reports 13, 1. (1958)

(71) Huang, X. Gao, C. Han, Y. Li, M. He, C. Hao, A. Zhang, D. Yu, C. Zou, G. Ma, Y. "Finite element analysis of resistivity measurement with van der Pauw method in a diamond anvil cell" App. Phys. Lett. 90, 242102. (2007)

(72) Kunderaci, M. Al-Sharab, J. Amatucci, G. "High-Power Nanostructured LiMn2-xNixO4 High-Voltage Lithium-Ion Battery Electrode Materials: Electrochemical Impact of Electronic Conductivity and Morphology" *Chem. Mat.* 18, 3585-3592. (2006)

(73) Gaines, L. Cuenca, R, "Costs of Lithium-Ion Batteries for Vehicles" *Center for Transportation Research, Argonne National Laboratory.* ANL/ESD-42. (2000)